









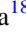


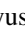

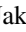
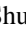




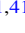

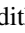


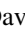





BASS. XXXIV. A Catalog of the Nuclear Millimeter-wave Continuum Emission Properties of AGNs Constrained on Scales $\leq 100\text{--}200$ pc

Taiki Kawamuro^{1,2,3,41} , Claudio Ricci^{1,4} , Richard F. Mushotzky⁵ , Masatoshi Imanishi^{2,6} , Franz E. Bauer^{7,8,9} ,
Federica Ricci^{10,11,12} , Michael J. Koss¹³ , George C. Privon^{14,15,16} , Benny Trakhtenbrot¹⁷ , Takuma Izumi^{2,6,42} ,
Kohei Ichikawa^{18,19,20} , Alejandra F. Rojas^{1,21,41} , Krista Lynne Smith^{22,23,43} , Taro Shimizu²⁴ , Kyuseok Oh²⁵ ,
Jakob S. den Brok^{26,27} , Shunsuke Baba²⁸ , Mislav Balokovic^{29,30} , Chin-Shin Chang³¹ , Darshan Kakkad^{32,33} ,
Ryan W. Pfeifle³⁴ , Matthew J. Temple^{1,41} , Yoshihiro Ueda³⁵ , Fiona Harrison³⁶ , Meredith C. Powell³⁷ ,
Daniel Stern³⁸ , Meg Urry³⁹ , and David B. Sanders⁴⁰ 

¹ Núcleo de Astronomía de la Facultad de Ingeniería, Universidad Diego Portales, Av. Ejercito Libertador 441, Santiago, Chile; taiki.kawamuro@mail.udp.cl

² National Astronomical Observatory of Japan, Osawa, Mitaka, Tokyo 181-8588, Japan

³ RIKEN Cluster for Pioneering Research, 2-1 Hirosawa, Wako, Saitama 351-0198, Japan

⁴ Kavli Institute for Astronomy and Astrophysics, Peking University, Beijing 100871, People's Republic of China

⁵ Department of Astronomy, University of Maryland, College Park, MD 20742, USA

⁶ Department of Astronomy, School of Science, Graduate University for Advanced Studies (SOKENDAI), 2-21-1 Osawa, Mitaka, Tokyo 181-8588, Japan

⁷ Instituto de Astrofísica and Centro de Astroingeniería, Facultad de Física, Pontificia Universidad Católica de Chile, Casilla 306, Santiago 22, Chile

⁸ Millennium Institute of Astrophysics (MAS), Nuncio Monseñor Sótero Sanz 100, Providencia, Santiago, Chile

⁹ Space Science Institute, 4750 Walnut Street, Suite 205, Boulder, CO 80301, USA

¹⁰ Dipartimento di Fisica e Astronomia, Università di Bologna, via Gobetti 93/2, I-40129 Bologna, Italy

¹¹ INAF Osservatorio Astronomico di Bologna, via Gobetti 93/3, I-40129 Bologna, Italy

¹² Dipartimento di Matematica e Fisica, Università degli Studi Roma Tre, Via della Vasca Navale 84, I-00146 Roma, Italy

¹³ Eureka Scientific, 2452 Delmer Street Suite 100, Oakland, CA 94602-3017, USA

¹⁴ National Radio Astronomy Observatory, 520 Edgemont Road, Charlottesville, VA 22903, USA

¹⁵ Department of Astronomy, University of Florida, P.O. Box 112055, Gainesville, FL 32611, USA

¹⁶ Department of Astronomy, University of Virginia, 530 McCormick Road, Charlottesville, VA 22904, USA

¹⁷ School of Physics and Astronomy, Tel Aviv University, Tel Aviv 69978, Israel

¹⁸ Frontier Research Institute for Interdisciplinary Sciences, Tohoku University, Sendai 980-8578, Japan

¹⁹ Astronomical Institute, Tohoku University, Aramaki, Aoba-ku, Sendai, Miyagi 980-8578, Japan

²⁰ Max-Planck-Institut für extraterrestrische Physik (MPE), Giessenbachstrasse 1, D-85748 Garching bei München, Germany

²¹ Centro de Astronomía (CITEVA), Universidad de Antofagasta, Avenida Angamos 601, Antofagasta, Chile

²² KIPAC at SLAC, Stanford University, Menlo Park, CA 94025, USA

²³ Southern Methodist University, Department of Physics, Dallas, TX 75205, USA

²⁴ Department of Physics and Astronomy, University College London, Gower Street, London WC1E 6BT, UK

²⁵ Korea Astronomy and Space Science Institute, Daedeokdae-ro 776, Yuseong-gu, Daejeon 34055, Republic of Korea

²⁶ Institute for Particle Physics and Astrophysics, ETH Zürich, Wolfgang-Pauli-Strasse 27, CH-8093 Zürich, Switzerland

²⁷ Argelander Institute for Astronomy, Auf dem Hügel 71, D-53231 Bonn, Germany

²⁸ Graduate School of Science and Engineering, Kagoshima University, Korimoto, Kagoshima, Kagoshima 890-0065, Japan

²⁹ Yale Center for Astronomy & Astrophysics, 52 Hillhouse Avenue, New Haven, CT 06511, USA

³⁰ Department of Physics, Yale University, P.O. Box 208120, New Haven, CT 06520, USA

³¹ Joint ALMA Observatory, Alonso de Cordova 3107, Vitacura, Santiago, Chile

³² European Southern Observatory, Alonso de Cordova 3107, Vitacura, Casilla 19001, Santiago de Chile, Chile

³³ European Southern Observatory, Karl-Schwarzschild-Strasse 2, Garching bei München, Germany

³⁴ Department of Physics & Astronomy, George Mason University, 4400 University Drive, MSN 3F3, Fairfax, VA 22030, USA

³⁵ Department of Astronomy, Kyoto University, Kyoto 606-8502, Japan

³⁶ Cahill Center for Astronomy and Astrophysics, California Institute of Technology, Pasadena, CA 91125, USA

³⁷ Institute of Particle Astrophysics and Cosmology, Stanford University, 452 Lomita Mall, Stanford, CA 94305, USA

³⁸ Jet Propulsion Laboratory, California Institute of Technology, 4800 Oak Grove Drive, MS 169-224, Pasadena, CA 91109, USA

³⁹ Yale Center for Astronomy & Astrophysics, Physics Department, New Haven, CT 06520, USA

⁴⁰ Institute for Astronomy, 2680 Woodlawn Drive, University of Hawaii, Honolulu, HI 96822, USA

Received 2022 July 5; revised 2023 August 9; accepted 2023 August 23; published 2023 November 2

Abstract

We present a catalog of the millimeter-wave (mm-wave) continuum properties of 98 nearby ($z < 0.05$) active galactic nuclei (AGNs) selected from the 70 month Swift/BAT hard-X-ray catalog that have precisely determined X-ray spectral properties and subarcsecond-resolution Atacama Large Millimeter/submillimeter Array Band 6 (211–275 GHz) observations as of 2021 April. Due to the hard-X-ray (>10 keV) selection, the sample is nearly unbiased for obscured systems at least up to Compton-thick-level obscuration, and provides the largest number of AGNs with high-physical-resolution mm-wave data ($\lesssim 100\text{--}200$ pc). Our catalog reports emission peak

⁴¹ FONDECYT postdoctoral fellow.

⁴² NAOJ fellow.

⁴³ Einstein fellow.



Original content from this work may be used under the terms of the [Creative Commons Attribution 4.0 licence](https://creativecommons.org/licenses/by/4.0/). Any further distribution of this work must maintain attribution to the author(s) and the title of the work, journal citation and DOI.

coordinates, spectral indices, and peak fluxes and luminosities at 1.3 mm (230 GHz). Additionally, high-resolution mm-wave images are provided. Using the images and creating radial surface brightness profiles of mm-wave emission, we identify emission extending from the central sources and isolated blob-like emission. Flags indicating the presence of these emission features are tabulated. Among 90 AGNs with significant detections of nuclear emission, 37 AGNs ($\approx 41\%$) appear to have both or one of extended or blob-like components. We, in particular, investigate AGNs that show well-resolved mm-wave components and find that these seem to have a variety of origins (i.e., a jet, radio lobes, a secondary AGN, stellar clusters, a narrow-line region, galaxy disk, active star formation regions, or AGN-driven outflows), and some components have currently unclear origins.

Unified Astronomy Thesaurus concepts: [Active galactic nuclei \(16\)](#); [Millimeter astronomy \(1061\)](#); [Galactic center \(565\)](#); [High energy astrophysics \(739\)](#); [Astrophysical black holes \(98\)](#)

Supporting material: figure sets, machine-readable tables

1. Introduction

Emission from active galactic nuclei (AGNs) has been identified over a wide range of wavelengths, from radio to γ -rays. However, the millimeter-wave (mm-wave) emission of AGNs is still poorly constrained, as indicated by the fact that mm-wave data points were rarely presented in typical AGN spectral energy distributions (SEDs; e.g., Elvis et al. 1994; Ho 2008; Hickox & Alexander 2018). Previous studies have suggested that the mm-wave emission cannot be explained simply by the extrapolation of a centimeter-wave (cm-wave) radio component (hereafter, “radio” indicates centimeter wave, or frequency below 30 GHz) or that of an infrared (IR) one (e.g., Behar et al. 2015; Inoue & Doi 2018; Inoue et al. 2020). It has been then proposed that the mm-wave component could be due to self-absorbed synchrotron emission from a compact region on a scale of $\lesssim 10^{-3}$ pc (e.g., Laor & Behar 2008; Inoue & Doi 2018; Inoue et al. 2020). Thus, the study of mm-wave AGN emission could be essential to obtain a complete picture of the AGN process (García-Burillo et al. 2021; Ricci et al. 2023).

To identify and better understand AGN-related mm-wave continuum emission, we systematically analyzed high angular resolution ($< 1''$) Atacama Large Millimeter/submillimeter Array (ALMA) Band 6 (211–275 GHz) data of 98 nearby AGNs ($z < 0.05$; Kawamuro et al. 2022, hereafter Paper I). The sample was created based on AGNs detected in the 70 month Swift/Burst Alert Telescope (BAT) hard-X-ray catalog (Baumgartner et al. 2013), which is nearly unbiased for obscured AGNs, at least up to the Compton-thick level of $N_{\text{H}} \approx 10^{24} \text{ cm}^{-2}$ (e.g., Burlon et al. 2011; Ricci et al. 2015) and has been used in various types of research (e.g., Kawamuro et al. 2013, 2016a, 2016b; Ricci et al. 2017a; Koss et al. 2018; Tanimoto et al. 2018; Baloković et al. 2020; Chiaraluce et al. 2020; Fischer et al. 2021). Our sample provides improvement with respect to previous samples used to study mm-wave emission (e.g., Behar et al. 2015, 2018) in two different aspects: (i) the angular resolutions of our data are basically less than $0''.6$, corresponding to $\lesssim 100$ – 200 pc for our targets, and are at least a few times better than those of the previous studies relying on $\sim 1''$ – $2''$ resolutions. The higher resolutions reduce contaminating light from star formation (SF) processes in the host galaxies (e.g., thermal emission from dust heated by stellar radiation, free-free emission from H II regions, and synchrotron emission from supernova remnants and other stellar processes; Condon 1992; Panessa et al. 2019); and (ii) the sample size is more than 3 times larger than the previous ones (Behar et al. 2015, 2018), which allows us to study the dependence of mm-wave emission on various parameters.

In Paper I, we discovered tight correlations of nuclear peak mm-wave luminosity with AGN luminosities (bolometric, AGN mid-infrared (MIR), 2–10 keV, and 14–150 keV luminosities). Among these correlations, that with the 14–150 keV luminosity has the smallest scatter (0.36 dex), comparable with that observed between $12 \mu\text{m}$ and X-ray luminosities (e.g., Gandhi et al. 2009). Focusing only on AGNs with the least amount of SF contamination, selected based on mm-wave spectral indices inconsistent with SF processes, we found a similar correlation to that obtained for the whole sample. This could indicate that, basically, a significant fraction of the observed mm-wave emission is related to the AGN activity traced by the X-ray emission.

Paper I focused on discussing the nuclear peak emission and its relations with AGN and host-galaxy properties, and this paper (Paper II, hereafter) presents a catalog of the mm-wave continuum properties of the 98 AGNs. For each object with significant detection of peak mm-wave emission, we provide its R.A. and decl., spectral index, and flux and luminosity at 1.3 mm (230 GHz). Furthermore, we show high-resolution mm-wave images of the sample. The images allowed us to identify objects that have resolved emission. These objects were classified, depending on the morphologies of the resolved mm-wave emission, and we present brief discussions on some of them in the context of the existing literature.

This paper is structured as follows. In Section 2, we introduce our AGNs, their basic properties, and their ALMA data. These pieces of information are summarized in Tables 1 and 2 in Appendix A. In Section 3, we describe our analysis of the ALMA Band 6 data and the identification of peak emission most likely related to an AGN. More details on the analysis were reported in Paper I. The derived mm-wave properties of the peak emission are available from Table 3. In addition, we describe our quantitative and systematic identification of resolved mm-wave components based on high-resolution images and radial surface brightness profiles, which are displayed in Figures 5 and 6, respectively. In Section 4, we then summarize the possible origins inferred for particularly well-resolved components. The summary is based on discussions for individual objects, presented in Appendix C. Finally, in Section 5, we give our conclusions.

Throughout the article, we adopt standard cosmological parameters ($H_0 = 70 \text{ km s}^{-1} \text{ Mpc}^{-1}$, $\Omega_{\text{m}} = 0.3$, and $\Omega_{\Lambda} = 0.7$).

2. Sample and Data

Our sample includes all nearby ($z < 0.05$) 70 month BAT AGNs in Baumgartner et al. (2013) with X-ray spectral properties precisely determined by Ricci et al. (2017b) and with

subarcsecond-resolution Band 6 (211–275 GHz) ALMA data, publicly available as of 2021 April. We focused on ALMA Band 6 because self-absorbed synchrotron emission from an AGN was expected to be more prominent at frequencies $\gtrsim 100$ –300 GHz (Inoue & Doi 2018; Inoue et al. 2020), and the band provided the largest sample of sources with $\gtrsim 100$ GHz data between Band 3 and Band 10. When searching the ALMA archive database, we considered a radius of $5''$ around BAT AGNs at $z < 0.05$. The radius corresponds to half of the radius of a typical size of the primary beam of the ALMA 12 m array in Band 6 ($\sim 20''$). We note that some BAT AGNs were identified by Koss et al. (2022a) as blazar-like objects, i.e., those with SEDs being dominated by nonthermal emission from radio to γ -rays and with radio properties being consistent with relativistic beaming. Specifically, the authors referred to the Roma Blazar Catalog (BZCAT; Massaro et al. 2009) and the follow-up work by Paliya et al. (2019). Although four are located at $z < 0.05$ and decl. $< 40^\circ$, which is an upper decl. limit for ALMA observations, they had no publicly available Band 6 data and therefore are not included in our sample. In the second data release of the Swift BAT AGN Spectroscopic Survey (BASS DR2; Koss et al. 2022a), there are 364 AGNs at $z < 0.05$ which are not blazar-like objects and can be observed by ALMA (i.e., decl. $< 40^\circ$), and among them, 98 AGNs (i.e., $\approx 27\%$ of the parent sample) had available ALMA data taken at subarcsecond resolution and were selected for our study.

Table 1 in Appendix A summarizes the basic information of our objects: the identification number assigned to each AGN in our works (Papers I and II), the BAT index in the 70 month catalog, Swift/BAT and counterpart names, the position of the AGN (R.A. and decl. in the International Celestial Reference System (ICRS) frame), the reference for the position, the redshift (z), the distance (D), and the Seyfert type. The AGN positions are detailed in Section 3.2. The distance measures (i.e., z and D) and Seyfert types were taken from the BASS DR2 database (Koss et al. 2022a, 2022b). We note that redshift-independent distances are adopted for objects at distances below 50 Mpc as the effect of peculiar velocity is expected to be significant compared to the recession velocity. For the distances, Koss et al. (2022a, 2022b) referred to the Extragalactic Distance Database of Tully et al. (2009), a catalog of the Cosmicflows project (Courtois et al. 2017), and the NASA/IPAC extragalactic database.⁴⁴

Our sample covers wide ranges in luminosity ($40 \lesssim \log(L_{14-150}/(\text{erg s}^{-1})) \lesssim 45$), black hole mass ($5 \lesssim \log(M_{\text{BH}}/M_\odot) \lesssim 10$), and Eddington ratio ($-4 \lesssim \log \lambda_{\text{Edd}} \lesssim 2$). In spite of our limit of $z = 0.05$, or $D \sim 200$ Mpc, the sample consists of 81 objects at distances below 100 Mpc. Also, according to the HyperLeda database (Makarov et al. 2014),⁴⁵ 55 and 36 objects are hosted by late-type and early-type galaxies, respectively. The host galaxies of the other seven objects were uncertain. Regarding the nuclear type, 33, 23, and 42 objects were classified by Koss et al. (2022a) as type-1, type-1.9, and type-2 AGNs, respectively. As inferred from these optical classifications, more than half, or 59 objects, are obscured with line-of-sight column densities above 10^{22} cm^{-2} . Finally, we remark that our sample includes some well-studied nearby AGNs at different wavelengths, such as NGC 1068,

NGC 1365, NGC 3783, NGC 4395, NGC 4945, IC 4329A, the Circinus Galaxy, NGC 5643, NGC 6240, and IC 5063. More details on our sample are described in Paper I.

In order to investigate AGN-related emission in Paper I by minimizing the impact of host-galaxy contamination, we carefully selected the high-resolution ALMA data. Initially, we compiled a list of publicly available subarcsecond-resolution data as of 2021 April. Then, for objects observed in multiple projects, we selected only the data from the project that provided the highest angular resolution. Moreover, as some projects comprised different group observation unit set (OUS) IDs, each indicating the need to merge the data, in these cases, we exclusively utilized the data with the group OUS ID that offered the highest resolution. Exceptionally, for NGC 424, we selected the second-highest-resolution data, because the highest data show many spurious lines in the spectra.

The information on the ALMA data we analyzed is summarized in Table 2 in Appendix A. The table lists the ALMA project code, member OUS ID, observing mode (mosaic or not), field of view (FOV), exposure time, and observation date, which were taken from the ALMA archive database. Maximum recoverable scales (MRSs), listed as well, were calculated from calibrated data by considering the fifth percentile of the projected baseline lengths of the antennas. In addition, we list the beam sizes along the minor and major axes, achieved with a weighting method applied during the cleaning process (see Section 3.1), and their physical scales for the object distances.

3. ALMA Data Analysis

3.1. Continuum Image Generation

We reconstructed mm-wave continuum emission images from the ALMA data using the Common Astronomy Software Applications package (CASA; McMullin et al. 2007). The raw data were reduced and calibrated by running scripts provided by the ARC in CASA with the versions adopted to create the scripts. For the rest of the analysis, we used CASA v.6.10.118. By considering only channels devoid of any strong emission lines, continuum emission was imaged not only for each spectral window, but also by combining all available spectral windows. In these imaging processes, we utilized the task `tclean` along with the deconvolver `clark` and the Briggs weighting method employing `robust = 0.5`. `clark` was adopted rather than the often-used alternative one `hogbom`, because the former properly subtracts clean components in the visibility space and also is faster, having enabled us to reconstruct images efficiently. The `robust` value does not offer the highest resolution nor the best sensitivity, but we opted for it. This is because we were able to preserve nearly the highest resolution while retaining a sensitivity close to the case of `robust = 2.0`, which provides the lowest noise level. However, if no significant emission was detected from a target, we reanalyzed its data adopting `robust = 2.0`. The details are described later. If data were obtained in the mosaic observation mode, we set `gridded` to `mosaic`. The `cell` size was set so that $\text{cell} < 1/3 \times \theta_{\text{beam}}^{\text{min}}$, where $\theta_{\text{beam}}^{\text{min}}$ is the FWHM of the beam size along the minor axis. The `threshold` parameter was also set so that $3\sigma_{\text{mm}} < \text{threshold} < 4\sigma_{\text{mm}}$, where σ_{mm} is the noise level derived from a region free from mm-wave emission. Finally, a primary-beam correction was applied to

⁴⁴ The NASA/IPAC Extragalactic Database (NED) is funded by the National Aeronautics and Space Administration and operated by the California Institute of Technology (<https://doi.org/10.26132/NED1>).

⁴⁵ <http://leda.univ-lyon1.fr/>

all reconstructed images. Here, we mention that we exceptionally performed a self-calibration process for NGC 1068 and Circinus galaxy, as fringe-like features were clearly left in the images without this calibration. According to the ALMA technical handbook,⁴⁶ flux densities measured in Band 6 can have a systematic uncertainty of 10%, and this is taken into consideration throughout this paper.

3.2. Nuclear Millimeter-wave Source Detection

To identify mm-wave emission possibly associated with an AGN in each constructed ALMA image, we first created a list of AGN positions (R.A. and decl.) using data and catalogs at different wavelengths. As X-ray emission is one of the best probes for AGN activity, we primarily relied on 3–7 keV images created by using Chandra data, which provide the highest resolution in the X-ray band. For 56 objects, we found on-axis Chandra data where the separation angle between the target and the focal plane is less than 1'. According to the Chandra X-Ray Center,⁴⁷ the positional accuracy is 1".4 at the 99% level for such on-axis observations. Therefore, for each target, we searched for a mm-wave peak within the 1".4 radius around a Chandra-based AGN position. As thresholds of 3–4 σ_{mm} were adopted for the cleaning processes, only emission whose flux density per beam was greater than 5 σ_{mm} was considered a detection.

For the 42 objects that did not have Chandra data, we considered the IR ($\approx 3\text{--}22\ \mu\text{m}$) ALLWISE catalog (Wright et al. 2010; Mainzer et al. 2011), which includes all our targets. In the IR band, the AGN position can be inferred from the observation of dust emission due to an AGN (e.g., Gandhi et al. 2009; Wright et al. 2010). The positional accuracy of the catalog was estimated to be $\approx 0".3$ by crossmatching with the Two Micron All Sky Survey (2MASS) catalog,⁴⁸ but we adopted 1".5 as a search radius for Wide-field Infrared Survey Explorer (WISE) positions. This is because the 2MASS accuracy for a peak, or the nucleus, of a spatially resolved galaxy at the 99% limit was estimated to be $\sim 1".5$ (She et al. 2017).

We adopted the mm-wave peaks identified by Chandra and WISE, basically in this order of priority, as candidates that are associated with AGNs. Further details can be found in Paper I. As a result, we identified significant ($>5\sigma_{\text{mm}}$) nuclear peaks for 89 AGNs, corresponding to a high detection rate of $\approx 91\%$.

For the nine objects without significant mm-wave peak detections, we performed the cleaning process with `robust = 2`. As a result, only for IC 4709, significant emission with $S_{\nu, \text{mm}}^{\text{peak}}/\sigma_{\text{mm}} = 7.2$ was identified ($S_{\nu, \text{mm}}^{\text{peak}}/\sigma_{\text{mm}} = 4.9$ for `robust = 0.5`). By considering this detection, mm-wave emission was detected from 90 AGNs (i.e., the detection fraction is 92%). As the last attempt to detect emission from the eight remaining objects, we proceeded to the analysis of alternative subarcsecond-resolution data. Eventually, even with the newly adopted data, no significant signal was found for the eight objects.

In Table 1, we list the positions of the identified mm-wave peaks as AGN positions. For the objects without significant mm-wave detections, we list AGN positions at different

wavelengths. Figure 5 of Appendix B summarizes the 98 images centered at these AGN positions.

3.3. Nonnuclear Millimeter-wave Components

The high-resolution ALMA observations ($\lesssim 0".6$, or $\lesssim 100\text{--}200$ pc) can reveal mm-wave emission that cannot be explained by a central unresolved source. The capability can be seen in Figure 1, where NGC 526A appears to show only an unresolved component, while NGC 3281, NGC 3393, and IC 5063 have other components. In the following, we refer to such resolved emission as nonnuclear emission, and in the next subsection, we describe our analyses for identifying nonnuclear components.

3.3.1. Quantitative and Systematic Identification of Nonnuclear Millimeter-wave Components

We quantitatively identified nonnuclear components that extended from central unresolved sources by deriving radial surface brightness profiles. Specifically, we defined concentric annuli centered on the nuclear emission peak. The radial width of each annulus was set to half of the average beam size of $\theta_{\text{beam}}^{\text{ave}} = (\theta_{\text{beam}}^{\text{min}} \times \theta_{\text{beam}}^{\text{maj}})^{1/2}$, and the outer radius was set to $15 \times \theta_{\text{beam}}^{\text{ave}}$. We then derived the averaged surface brightnesses ($S_{\nu, \text{mm}}^{\text{ave}}$ in units of Jy beam^{-1}) for all annuli using the `imstat` task. To confirm whether mm-wave emission is an excess over a central unresolved source that extends by the point-spread function (PSF), we also calculated the surface brightnesses of the achieved synthesized beam for the same annuli. Then, for comparison, the brightness in the innermost circle was adjusted to the observed one. As examples, Figure 2 shows observed radial profiles and adjusted synthesized-beam ones for the four objects mentioned previously (i.e., NGC 526A, NGC 3281, NGC 3393, and IC 5063). The profiles for all 98 AGNs are displayed in Figure 6 in Appendix B. For NGC 526A, no significant excess is found, consistent with the visual inspection; nonnuclear components do not exist. In contrast, the profile for NGC 3281 infers the presence of significant extended emission with respect to the unresolved component above three times the standard error (SE). We used the obtained radial profiles for identifying such emission extending from the central unresolved component, and labeled AGNs for which significant extended components were confirmed with an ‘‘e.’’ Besides the extended emission, blob-like emission, which we define as emission separated from the central emission, can be seen in some objects. Clear examples are NGC 3393 and IC 5063, as seen in Figure 1. The blob-like features of IC 5063 are significantly detected also in its radial profile around the range $\theta_{\text{beam}}^{\text{ave}} \sim 4\text{--}6$ (Figure 2), while the blob-like component of NGC 3393 becomes ambiguous in the radial profile around $\theta_{\text{beam}}^{\text{ave}} = 2\text{--}4$. This is likely due to noise in the same annulus, and indicates that, in the radial profile, we can easily miss significant blob-like components. We thus identified blob-like components in an alternative simple way: an image with 5σ contours was created, and then any components that were isolated from the central emission enclosed by the $5\sigma_{\text{mm}}$ contour and were significant above $5\sigma_{\text{mm}}$ were systematically regarded as blob-like components. We labeled AGNs for which blob-like components were found with a ‘‘b.’’

With the two flags, e and b, NGC 3281, NGC 3393, and IC 5063, shown in Figure 1, were labeled with e, b, and b, while no flag was raised for NGC 526A. Of the 90 AGNs, 37 AGNs

⁴⁶ <http://almascience.org/documents-and-tools/cycle8/alma-technical-handbook>

⁴⁷ <https://exc.harvard.edu/cal/ASPECT/celmon/>

⁴⁸ https://wise2.ipac.caltech.edu/docs/release/allsky/expsup/sec6_4.html

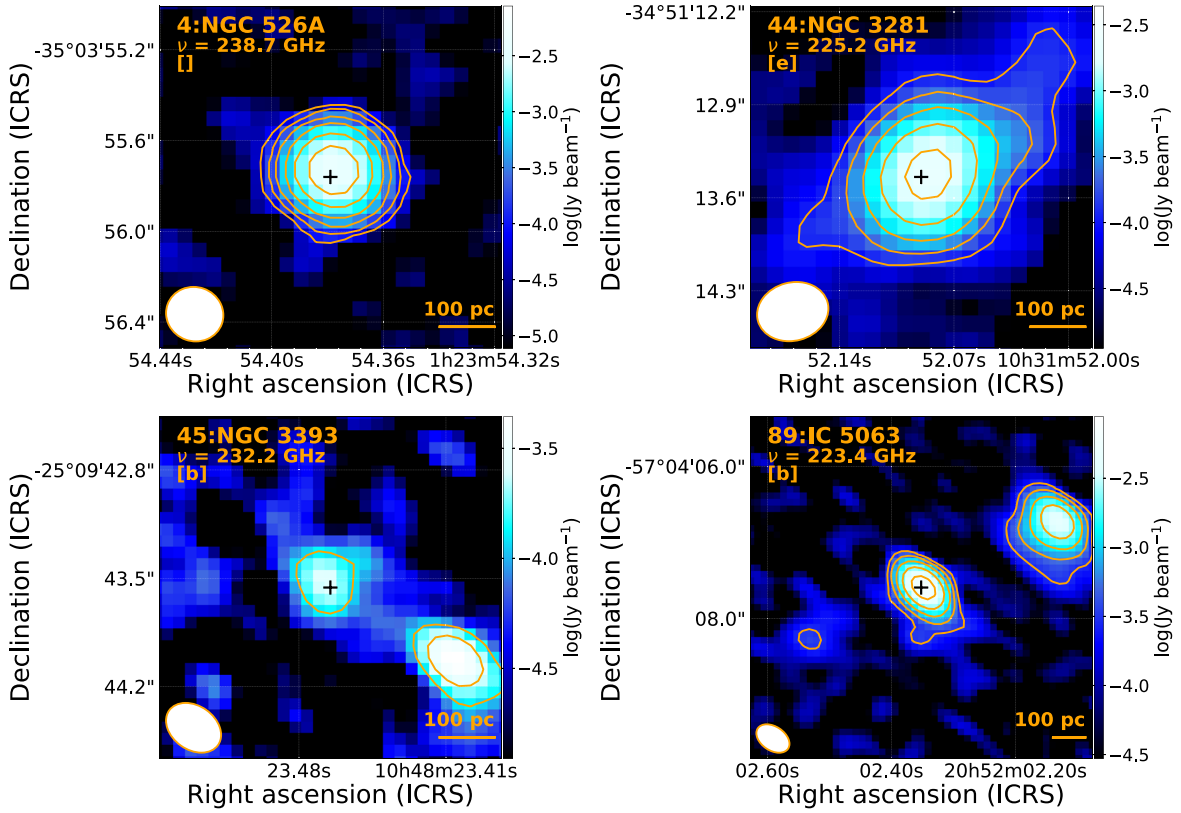


Figure 1. ALMA Band 6 images for NGC 526A, NGC 3281, NGC 3393, and IC 5063. The beam sizes are indicated by the white ellipses in the bottom-left corners. In each panel, the identification number, assigned in this study (Table 1) and Paper I, is presented along with the object name. The frequency is the rest-frame central frequency of the collapsed spectral window adopted, after removing any emission line flux. The central black cross indicates the peak of the nuclear mm-wave emission, expected to be the AGN position. A morphological parameter, which can consist of e and b, is also presented below the frequency. As detailed in Section 4, e and b indicate the presence of extended emission connected with the central unresolved component and the presence of isolated blob-like emission, respectively. Colors are assigned according to flux density per beam following the color bar on the right side. The orange contours indicate where flux densities per beam are $5\sigma_{\text{mm}}$, $10\sigma_{\text{mm}}$, $20\sigma_{\text{mm}}$, $40\sigma_{\text{mm}}$, $80\sigma_{\text{mm}}$, and $160\sigma_{\text{mm}}$. For NGC 526A, NGC 3281, NGC 3393, and IC 5063, $\sigma_{\text{mm}} = 0.016$ mJy beam $^{-1}$, $\sigma_{\text{mm}} = 0.022$ mJy beam $^{-1}$, $\sigma_{\text{mm}} = 0.025$ mJy beam $^{-1}$, $\sigma_{\text{mm}} = 0.059$ mJy beam $^{-1}$, respectively. ALMA images for all 98 objects are summarized in Appendix B.

were quantitatively and systematically found to have non-nuclear emission, corresponding to $\approx 41\%$. The flags are tabulated in Table 3.

We warn readers that structures larger than an MRS are resolved out and therefore there should be nonnuclear emission that we missed. Indeed, we confirmed that the size of each identified nonnuclear component is less than the MRS of the data used for the identification.

While the identification of the nonnuclear components depends on whether there are actually nonnuclear components and also on the MRS as described above, some other observational properties can be factors that affect the identifiability. As possible properties, we investigated two parameters: the detection significance for peak emission and the physical resolution. The former was considered because we have defined peak emission as the nuclear component, and therefore nonnuclear emission around that (if any) is basically fainter and would not be detected for sources detected at low significance. The latter was based on the simple fact that a coarse resolution makes it difficult to resolve emission components. To assess these hypotheses, we created two samples: one consists of the 53 AGNs without any morphological flags and the other includes the other 37 AGNs with significant nonnuclear components. We refer to these samples as Sample-n and Sample-eb, respectively. Using the Kolmogorov–Smirnov test (K-S test), we then compared their

detection significance and beam size distributions, as shown in Figure 3. The K-S test rejects their similarities with p -values of $P_{\text{KS}} \approx 7.9 \times 10^{-4}$ and $P_{\text{KS}} \approx 2.3 \times 10^{-7}$, respectively. Also, judging from the distributions in Figure 3, we confirmed that the Sample-n objects were detected at lower significances and were observed at coarser physical resolutions, as expected.

3.4. Millimeter-wave Spectral Indices

3.4.1. Caution on Spectral Indices

Based on the ALMA data used for the imaging, we estimated the spectral index α_{mm} (defined as $S_{\nu, \text{mm}}^{\text{peak}} \propto \nu^{-\alpha_{\text{mm}}}$). The data are optimized to produce high-resolution images, but are not well suited for estimating this index, for example, due to the narrow aggregate bandwidth (< 4 GHz). Therefore, we emphasize that there is a large uncertainty in each index, especially in the case where the signal-to-noise ratio of the nuclear emission is low ($\lesssim 50$).

3.4.2. Actual Derivation

The spectral index is necessary to derive the fundamental parameters of luminosity and flux. The k -corrected luminosity can be derived using the equation below

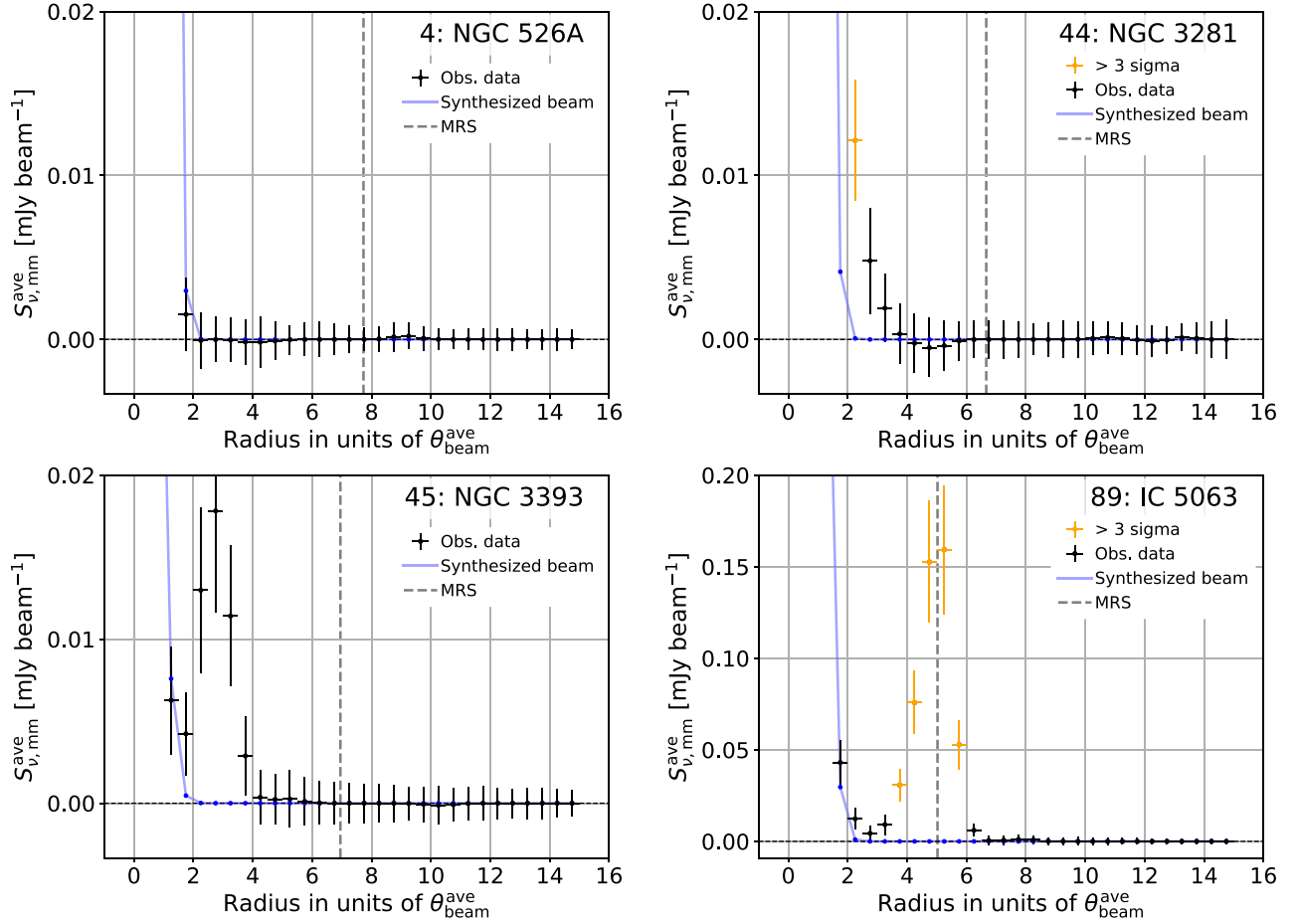


Figure 2. Radial surface-brightness profiles for NGC 526A, NGC 3281, NGC 3393, and IC 5063. The radius is in units of the averaged beam size ($\theta_{\text{beam}}^{\text{ave}}$). In each panel, observed values are indicated with black error bars, but particularly those detected at significances more than 3 times the SEs with respect to an unresolved component (blue dots and lines) are shown in orange. The dashed gray line indicates the MRS. The ALMA images of the four objects are presented in Figure 1. The radial profiles for all 98 AGNs are summarized in Figure 6.

(e.g., Novak et al. 2017):

$$\nu L_{\nu, \text{mm}}^{\text{peak}} = \nu \frac{4\pi D^2}{(1+z)^{1-\alpha_{\text{mm}}}} \left(\frac{\nu}{\nu'}\right)^{-\alpha_{\text{mm}}} S_{\nu', \text{mm}}^{\text{peak}}, \quad (1)$$

where ν is set to 230 GHz, i.e., the representative frequency considered in this study, and $S_{\nu', \text{mm}}^{\text{peak}}$ is the peak flux density per beam at the observed frequency of ν' . Each flux density per beam was derived from an image consisting of all available spectral windows. By following the definition of the luminosity, the flux is defined as follows:

$$\nu F_{\nu, \text{mm}}^{\text{peak}} = \nu \frac{1}{(1+z)^{1-\alpha_{\text{mm}}}} \left(\frac{\nu}{\nu'}\right)^{-\alpha_{\text{mm}}} S_{\nu', \text{mm}}^{\text{peak}}. \quad (2)$$

While the effect of the k -correction is $\approx 0.8\%$ as the median value for the sample, it can be $\approx 5\%$ – 10% for six distant objects. This is comparable to the systematic uncertainty of $\sim 10\%$, and therefore the k -correction was applied uniformly.

To obtain the spectral index of α_{mm} and its error of $\Delta\alpha_{\text{mm}}$ necessary to calculate the luminosity and flux and their errors, we fitted a power-law function to the flux measurements from individual spectral windows based on the chi-square method. For 70 objects that were observed with more than two spectral windows and for which peak emission was detected in all

windows, the spectral index and statistical error were estimated. To the errors, we added a systematic uncertainty of 0.2, which takes into account a possible flux calibration uncertainty between spectral windows at ~ 230 GHz (Francis et al. 2020). The mean and standard dispersion of the indices of 68 sources whose indices were individually calculated are $\alpha_{\text{mm}} = 0.5 \pm 1.2$. Two objects, NGC 1068 and NGC 1194, were excluded from this calculation because their constraints could be unreliable, which is described in the paragraph after the next two; the actual indices assigned to the two objects to calculate $L_{\nu, \text{mm}}^{\text{peak}}$ and $F_{\nu, \text{mm}}^{\text{peak}}$ are also detailed therein. For the remaining 28 objects, the representative value of $\alpha_{\text{mm}} = 0.5 \pm 1.2$ was adopted to calculate their luminosities and fluxes.

We emphasize here that many objects, especially those with a low detection significance, have large uncertainties of ≥ 1 in their indices; the corresponding fraction is $\sim 40\%$. This is seen in Figure 4, where the indices are plotted as a function of signal-to-noise ratio of the nuclear mm-wave emission. Therefore, we caution that many of the estimates are not so reliable, and that additional data are important for more reliable estimates.

In addition to showing the above fact, Figure 4 suggests an interesting result that the indices are well distributed around a mean value of ≈ 0.5 . This suggests that the dust emission, for which a steep slope is expected (e.g., ~ -3 to ~ -4), is unlikely to

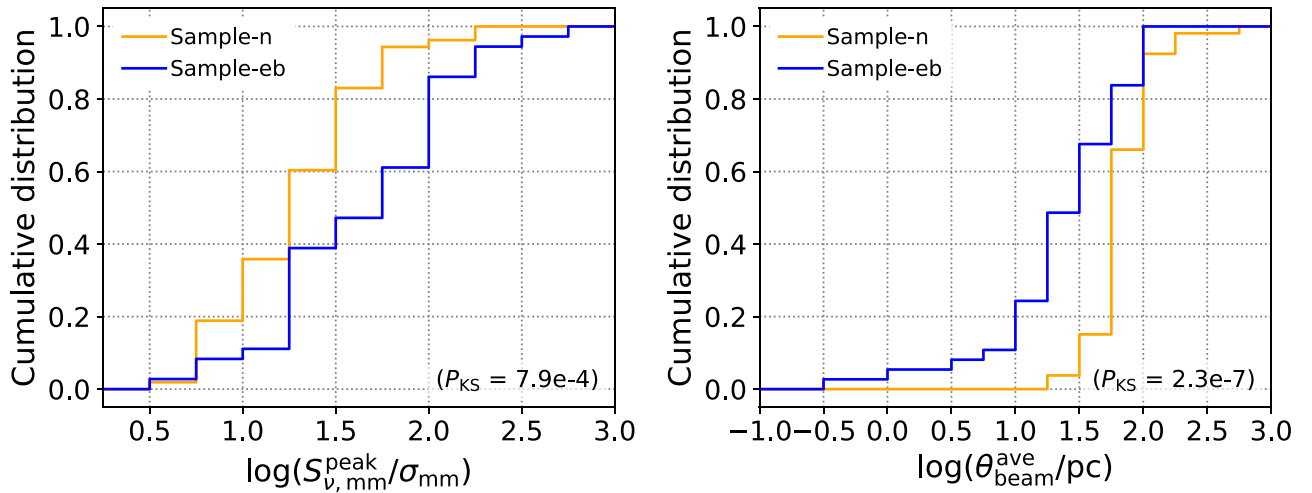


Figure 3. Left: cumulative detection-significance distribution of the objects showing both or one of extended (e) or blob-like (b) components (blue) and the others without such nonnuclear components (yellow). The p -value obtained from the K-S test is indicated in the parenthesis. The small p -value suggests the significant difference in the distributions and the trend that the objects without nonnuclear components were detected at lower significance. Right: same as the left, but for the beam size in units of parsecs. The distributions and p -value suggest the trend that the objects without nonnuclear components were observed at coarser physical resolutions.

be the dominant source, and flatter components, such as synchrotron and free-free emission, are likely to be more important.

Returning to NGC 1068, we find that its spectral index ($\alpha_{\text{mm}} = 1.5 \pm 0.3$ around 270 GHz) is largely different from an index of $\alpha_{\text{mm}} \sim -1.3$ expected from a mm-wave band SED constructed by Inoue et al. (2020), and also is a few sigma higher than the index more carefully derived by Michiyama et al. (2023) (i.e., $\alpha_{\text{mm}} \sim 0.5\text{--}0.8$). The latter study constructed an SED denser than that of Inoue et al. (2020) by using high-resolution ($\approx 0''.05$) ALMA data. First, as a possible cause, we considered that this discrepancy might be ascribed to our data having a narrower spacing between the lowest and highest frequency spectral channels than those for the others (i.e., ≈ 5.4 GHz with respect to $\sim 14\text{--}20$ GHz), except for NGC 1194. The object was also observed with a similar narrow spacing (≈ 4.9 GHz). To estimate the index better, we analyzed the second-highest-resolution data with $\theta_{\text{beam}}^{\text{ave}} \approx 0''.018$ and a wider spacing of ≈ 19 GHz. Then, a spectral index was constrained to be $\alpha_{\text{mm}} = 0.4 \pm 0.2$ around 260 GHz. We additionally analyzed Band 7 data with comparable resolution ($\approx 0''.018$) at 331 GHz (group OUS ID = A001/X1465/X212e in 2019.1.00854.S). We then found that the interband spectral index between the Band 6 and Band 7 frequencies (256 GHz and 331 GHz) also inferred $\alpha_{\text{mm}} \approx 0.4$. The two measurements disfavor the result of Inoue et al. (2020) but are virtually consistent with the updated one of Michiyama et al. (2023). Thus, the true spectral index is possibly ~ 0.4 , and it is suggested that the spectral index derived from the narrow spacing has a large systematic uncertainty. Eventually, for NGC 1068, we conservatively adopted the representative value of $\alpha_{\text{mm}} = 0.5 \pm 1.2$, consistent with the possible value of 0.4. For the remaining object NGC 1194, as this did not have other subarcsecond ALMA data, we also adopted the same representative value.

In addition to the narrow spectral coverage suspected as a cause of the unreliable constraint on the spectral index, we checked whether there were objects whose estimated indices could be unreliable due to observations with smaller aggregate bandwidths of < 3.75 GHz. As a result, it was confirmed that no

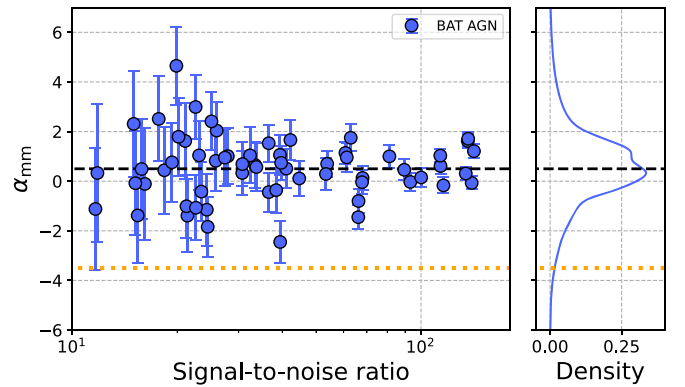


Figure 4. Spectral index as a function of the signal-to-noise ratio of the nuclear emission (left panel) and the density derived by the kernel density estimation (right panel). The black dashed lines correspond to 0.5, the mean for the BAT AGNs, while the yellow dotted lines indicate $\alpha_{\text{mm}} = -3.5$, expected for thermal dust emission.

objects were observed at such small aggregate bandwidths and have estimated indices.

Lastly, we attempted to improve the constraints on the spectral indices with large uncertainties of $\Delta\alpha_{\text{mm}} \geq 1$. For the 27 objects with $\Delta\alpha_{\text{mm}} \geq 1$, we searched for different subarcsecond-resolution Band 6 data, and found that only NGC 4388 had available data. With the data, the spectral index was constrained to be $\alpha_{\text{mm}} = -0.5 \pm 0.8$ around 220 GHz, while that obtained with the highest-resolution data was $\alpha_{\text{mm}} = 1.0 \pm 1.0$ at ~ 260 GHz. This apparently large difference could be ascribed, in part, to a synchrotron self-absorption component having a peak around these frequencies, as suggested for nearby AGNs (e.g., Inoue & Doi 2018; Inoue et al. 2020). Anyway, the derived luminosities and fluxes from the two different data sets differ by only ≈ 0.1 dex and are consistent within 1σ .

With the indices estimated from the highest-resolution data, we calculated the luminosities and fluxes. To their errors, we added a systematic uncertainty of 10%, as recommended by the ALMA technical handbook. Table 3 in Appendix A provides the mm-wave properties obtained for all objects in our sample (e.g., spectral indices, luminosities, and fluxes).

4. Nonnuclear Emission

Although the main purpose of this paper is to provide a catalog of the mm-wave properties derived in Paper I, we also discuss the origins of nonnuclear components found for some objects to obtain insights into the nonnuclear emission. This was omitted in Paper I to focus on discussing unresolved nuclear mm-wave components. Of the 37 objects having morphology flags (i.e., e and b), for further discussion, we select 28 objects that showed largely extended nonnuclear components, or quantitatively those with the number of annuli where emission was detected being more than two and/or with blob-like components. Here, we exclude three objects with the b flag (NGC 424, Ark 120, and H 0557–385), as their blob-like components were significant in only a few pixels and it is ambiguous whether they are real emission or not.

In Appendix C, we present our discussions on all the selected objects, and here only summarize our findings to avoid lengthy descriptions in the main text. Eventually, we have found that the nonnuclear components in the investigated objects are related to various mechanisms and regions, such as a jet and radio lobes (e.g., NGC 3393 and IC 5063), a secondary AGN (NGC 6240), stellar clusters (NGC 1365), a narrow-line region (e.g., IC 4518A), a galaxy disk (e.g., NGC 3281, NGC 4945, and NGC 5506), active SF (e.g., NGC 7130 and NGC 7469), or AGN-driven outflows (NGC 7582). Also, we have found that some objects (e.g., NGC 612, NGC 1566, IRAS 05189-2524, and NGC 3281) show components whose physical origins are unclear. In any case, further high-resolution observations are desired, perhaps unveiling unknown mm-wave emitting mechanisms.

5. Conclusions

This paper provides a catalog of the properties of mm-wave continuum emission for the 98 nearby AGNs ($z < 0.05$) selected from the 70 month Swift/BAT hard-X-ray catalog (Baumgartner et al. 2013; Ricci et al. 2017b). Thanks to the hard-X-ray selection, the sample is almost unbiased for obscured systems up to the Compton-thick level of absorption ($N_{\text{H}} \sim 10^{24} \text{ cm}^{-2}$). The mm-wave properties were constrained by a systematic analysis of the ALMA Band 6 (211–275 GHz) data taken at high resolutions of $\lesssim 0''.6$, corresponding to $\lesssim 100\text{--}200$ pc for almost all targets. Tables 1 and 2 summarize the basic properties of the objects (e.g., names, distances, and Seyfert types) and the ALMA data used (e.g., achieved resolutions), respectively. Then, Table 3 lists the derived mm-wave properties. As Paper I found, Table 3 lists the derived mm-wave properties. As Paper I found that the peak mm-wave emission may generally be produced by an AGN, this catalog could be used for various AGN studies, such as a study of AGN SEDs, including mm-wave emission, which has often been ignored in past studies. Furthermore, high-resolution mm-wave images are presented in Figure 5. Also, we derived the radial profiles of the observed surface brightnesses from the images, as summarized in Figure 6, and we systematically identified significant nonnuclear emission extending from the central source in Section 3.3.1. In addition, we systematically searched the original images for isolated blob-like mm-wave components. We then labeled AGNs that showed extended and blob-like components with “e” and “b,” respectively. Among the 90 AGNs with significant detections of nuclear mm-wave emission, both or one of extended (e) or blob-like (b) components were identified for 37 AGNs (i.e., $\approx 41\%$). In particular, for 28 AGNs that showed largely extended mm-wave components and/or blob-like

components, we have briefly discussed them, while referring to the existing literature in Appendix C. Various mechanisms and regions (e.g., a jet and radio lobes, a secondary AGN, stellar clusters, a narrow-line region, a galaxy disk, active SF, or AGN-driven outflows) were eventually inferred, while some mm-wave components had unknown origins. To understand the origin of these components better, further investigations of the individual objects are encouraged.

Acknowledgments

We thank the reviewer for the useful comments, which helped us improve the quality of the manuscript. We acknowledge support from FONDECYT Postdoctoral Fellowships 3200470 (T.K.), 3210157 (A.R.), and 3220516 (M.J.T.), FONDECYT Iniciacion grant 11190831 (C.R.), FONDECYT Regular 1200495 and 1190818 (F.E.B.), ANID BASAL project FB210003 (C.R. and F.E.B), and Millennium Science Initiative Program ICN12_009 (F.E.B). T.K., T.I., and M.I. are supported by JSPS KAKENHI grant Nos. JP20K14529/JP23K13153, JP20K14531, and JP21K03632, respectively. B.T. acknowledges support from the European Research Council (ERC) under the European Union’s Horizon 2020 research and innovation program (grant agreement 950533) and from the Israel Science Foundation (grant 1849/19). K.O. acknowledges support from the Korea Astronomy and Space Science Institute under the R&D program (Project No. 2023-1-868-03) supervised by the Ministry of Science and ICT, and the National Research Foundation of Korea (NRF-2020R1C1C1005462). M.B. acknowledges support from the YCAA Prize Postdoctoral Fellowship. The scientific results reported in this article are based on data obtained from the Chandra Data Archive. This research has used software provided by the Chandra X-ray Center (CXC) in the application packages CIAO. This paper uses the following ALMA data: ADS/JAO.ALMA #2012.1.00139.S, #2012.1.00474.S, #2013.1.00525.S, #2013.1.00623.S, #2013.1.01161.S, #2015.1.00086.S, #2015.1.00370.S, #2015.1.00597.S, #2015.1.00872.S, #2016.1.00254.S, #2016.1.00839.S, #2016.1.01140.S, #2016.1.01279.S, #2016.1.01385.S, #2016.1.01553.S, #2017.1.00236.S, #2017.1.00255.S, #2017.1.00395.S, #2017.1.00598.S, #2017.1.00886.L, #2017.1.00904.S, #2017.1.01439.S, #2018.1.00006.S, #2018.1.00037.S, #2018.1.00211.S, #2018.1.00248.S, #2018.1.00538.S, #2018.1.00576.S, #2018.1.00581.S, #2018.1.00657.S, #2018.1.00978.S, and #2019.1.01742.S. ALMA is a partnership of ESO (representing its member states), NSF (USA) and NINS (Japan), together with NRC (Canada), MOST and ASIAA (Taiwan), and KASI (Republic of Korea), in cooperation with the Republic of Chile. The Joint ALMA Observatory is operated by ESO, AUI/NRAO and NAOJ. Data analysis was in part carried out on the Multi-wavelength Data Analysis System operated by the Astronomy Data Center (ADC), National Astronomical Observatory of Japan. This publication makes use of data products from the Wide-field Infrared Survey Explorer, which is a joint project of the University of California, Los Angeles, and the Jet Propulsion Laboratory/California Institute of Technology, funded by the National Aeronautics and Space Administration. This research has made use of the NASA/IPAC Extragalactic Database, which is funded by the National Aeronautics and Space Administration and operated by the California Institute of Technology. This research has made use of the SIMBAD database, operated at CDS, Strasbourg, France. We acknowledge the usage of the HyperLeda database (<http://leda.univ-lyon1.fr>).

Appendix A Complete Tables

In this appendix, we present the complete tables of the basic properties of our 98 AGNs (Table 1), the ALMA data we used (Table 2), and the mm-wave properties (Table 3).

Table 1
Basic Properties of Our Targets

(1) <i>N</i>	(2) Index	(3) BAT Name	(4) Counterpart Name	(5) R.A. (deg)	(6) Decl. (deg)	(7) References	(8) <i>z</i>	(9) <i>D</i> (Mpc)	(10) ΔD (Mpc)	(11) Type
01	28	J0042.9–2332	NGC 235A	10.720029	–23.541049	A	0.02207	96.1	0.1(a)	1.9
02	31	J0042.9–1135	MCG–2–2–95	10.786582	–11.601037	W	0.01938	84.3	0.1(a)	2
03	58	J0111.4–3808	NGC 424	17.865171	–38.083467	A	0.01088	51.0	0.1(a)	1.9
04	72	J0123.8–3504	NGC 526A	20.976579	–35.065489	A	0.01890	82.1	0.1(a)	1.9
05	84	J0134.1–3625	NGC 612	23.490394	–36.493180	A	0.02990	131.0	0.1(a)	2
06	102	J0201.0–0648	NGC 788	30.276937	–6.815879	A	0.01365	59.1	0.1(a)	2
07	112B	J0209.5–1010D1	NGC 833	32.336852	–10.133077	W	0.01355	58.6	0.1(a)	2
08	112	J0209.5–1010D2	NGC 835	32.352549	–10.135861	W	0.01334	57.7	0.1(a)	2
09	131	J0231.6–3645	IC 1816	37.962408	–36.672156	A	0.01665	72.2	0.1(a)	2
10	134	J0234.6–0848	NGC 985	38.657667	–8.787805	A	0.04302	190.3	0.1(a)	1

Note. (1) Identification number in this paper (Paper II) and Paper I. (2) BAT index. (3), (4) BAT and counterpart names, taken from Ricci et al. (2017b). (5), (6) R.A. and decl. in units of degrees in the ICRS frame. (7) Reference for the position in (5), (6): A = ALMA (this work), W = ALLWISE (Wright et al. 2010; Mainzer et al. 2011), and CXO = Chandra (this work). (8) Redshift. (9), (10) Distance and its error in units of megaparsecs. Particularly for objects at distances below 50 Mpc, redshift-independent distances are adopted by referring to the Extragalactic Distance Database of Tully et al. (2009), a catalog of the Cosmicflows project (Courtois et al. 2017), and the NASA/IPAC Extragalactic Database in this order (see Koss et al. 2022a, for details). Also, we note that (a) indicates that a small redshift error of the order of 10 km s^{-1} , used in computing the distance error, results in a very small error of $\ll 0.1$ Mpc and thus 0.1 Mpc is denoted as a substitute. (11) Seyfert type. Information in the last four columns is taken from the BASS DR2 paper of Koss et al. (2022a) or the authors.

(This table is available in its entirety in machine-readable form.)

Table 2
Basic Information of the ALMA Data

(1) <i>N</i>	(2) Project code	(3) OUS ID	(4) Mosaic	(5) MRS (arcseconds)	(6) FOV (arcseconds)	(7) Exp. (s)	(8) Date	(9) $\theta_{\text{beam}}^{\text{maj}}$ (arcseconds)	(10) $\theta_{\text{beam}}^{\text{min}}$ (arcseconds)	(11) $\theta_{\text{beam,pc}}^{\text{maj}}$ (pc)	(12) $\theta_{\text{beam,pc}}^{\text{min}}$ (pc)
01	2018.1.00538.S	A001/X133d/X1fce	...	3.4	24.9	4990	2018-11-04	0.16	0.13	75	61
02	2018.1.00538.S	A001/X133d/X1fbe	...	4.0	24.9	2026	2018-10-26	0.33	0.24	130	99
03	2017.1.00236.S	A001/X1296/X91b	...	1.6	24.9	5685	2017-12-02	0.099	0.076	24	18
04	2018.1.00538.S	A001/X133d/X1fe8	...	3.8	24.8	1845	2018-10-22	0.25	0.24	100	94
05	2017.1.00904.S	A001/X1296/X5bd	...	0.80	25.1	435	2017-11-19	0.052	0.044	33	27
06	2018.1.00538.S	A001/X133d/X1ff0	...	4.5	26.3	514	2018-11-02	0.34	0.26	97	73
07	2018.1.00657.S	A001/X133d/X21f5	mosaic	6.0	168.8	78	2019-04-27	0.48	0.42	130	120
08	2018.1.00657.S	A001/X133d/X21f5	mosaic	6.0	168.8	78	2019-04-27	0.48	0.42	130	110
09	2018.1.00538.S	A001/X133d/X1fa4	...	4.2	26.3	1119	2018-10-26	0.31	0.28	100	99
10	2016.1.01140.S	A001/X87a/X78a	...	1.5	26.2	1089	2017-08-18	0.11	0.089	100	82

Note. (1) Identification number in this paper (Paper II) and Paper I. (2) ALMA project code. (3) Member OUS ID. (4) Observation mode (mosaic or not). (5) MRS in units of arcseconds, calculated from the calibrated data. (6) FOV in units of arcseconds. (7) Exposure time in units of seconds. (8) Observation date. Information in (6), (7), and (8) are taken from the ALMA archive database. (9), (10) Beam sizes (FWHM) in units of arcseconds along the major and minor axes. These are estimated from a reconstructed ALMA image for each target. (11), (12) Physical resolutions achieved in units of parsecs.

(This table is available in its entirety in machine-readable form.)

Table 3
Complete List of the mm-wave Properties

(1)	(2)	(3)	(4)	(5)	(6)	(7)	(8)	(9)	(10)	(11)	(12)	(13)	(14)	(15)
N	Det./SpN	$\nu_{\text{mm}}/\nu_{\text{mm}}^{\text{ent}}$	$W_{\text{mm}}/W_{\text{mm}}^{\text{ent}}$	$S_{\nu,\text{mm}}^{\text{peak}}$	σ_{mm}	$S_{\nu,\text{mm}}^{\text{peak}}/\sigma_{\text{mm}}$	f_{F} f_{L}	$\log \nu F_{\nu,\text{mm}}^{\text{peak}}$	$\log \nu L_{\nu,\text{mm}}^{\text{peak}}$	$\Delta \log \nu F_{\nu,\text{mm}}^{\text{peak}}$ $\Delta \log \nu L_{\nu,\text{mm}}^{\text{peak}}$	α_{mm}	$\Delta \alpha_{\text{mm}}$	f_{M}	N_{M}
		(GHz)	(GHz)	(mJy beam $^{-1}$)	(mJy beam $^{-1}$)			(erg cm $^{-2}$ s $^{-1}$)	(erg s $^{-1}$)	(erg cm $^{-2}$ s $^{-1}$) (erg s $^{-1}$)				
01	4/4	233.6/233.6	6.2/7.2	0.44	0.01	39	...	-14.99	39.06	0.05	1.1	0.8
02	0/4	234.3/234.3	6.1/7.2	0.05	0.02	2.8	<	-15.51	38.42
03	4/4	233.9/233.7	4.8/7.6	1.19	0.01	114	...	-14.56	38.93	0.04	0.6	0.3	eb	1
04	4/4	234.3/234.3	5.9/7.2	4.02	0.02	258	...	-14.03	39.88	0.04	0.7	0.2
05	4/4	232.2/232.4	6.3/7.8	22.38	0.07	300	...	-13.30	41.02	0.04	0.3	0.2	eb	4
06	4/4	221.7/221.7	6.1/7.2	0.36	0.03	12	...	-15.09	38.53	0.06	0	3
07	0/4	233.5/233.5	6.5/7.4	0.33	0.09	3.6	<	-14.72	38.89
08	0/4	233.5/233.5	6.2/7.4	0.18	0.09	2.0	<	-14.85	38.75
09	4/4	221.0/221.0	6.2/7.2	0.67	0.02	33	...	-14.83	38.97	0.05	0.7	0.9
10	4/4	222.0/222.0	5.6/7.9	1.22	0.02	54	...	-14.57	40.07	0.04	0.7	0.5

Note. (1) Identification number in this paper (Paper II) and Paper I. (2) The number of spectral windows where mm-wave emission was significantly detected and that of spectral windows used for the continuum detection. (3) Observed central frequency of the collapsed spectral window after removing any emission line flux and central frequency for the entire data. (4) Aggregate bandwidth used for continuum detections and bandwidth for the entire data. (5) Peak flux density per beam in units of mJy beam $^{-1}$. (6) Noise level in units of mJy beam $^{-1}$. We note that this does not consider systematic uncertainties. We also note that the quantities in (5) and (6) were derived in the images after the primary-beam correction. (7) Significance of peak emission. (8) Flag for flux and luminosity. The "<" flag indicates that the flux and luminosity must be regarded as upper limits at the $5\sigma_{\text{mm}}$ level. (9), (10) Flux in units of erg cm $^{-2}$ s $^{-1}$ and luminosity in units of erg s $^{-1}$ on a log scale. (11) Uncertainties in the flux and luminosity. (12) Spectral index defined as $S_{\nu,\text{mm}}^{\text{peak}} \propto \nu^{-\alpha_{\text{mm}}}$. (13) Error in the spectral index. (14) Flag indicating what morphological components were identified in Section 4: e = extended emission and b = blob-like emission. (15) Number of annuli where significant nonnuclear emission was detected.

(This table is available in its entirety in machine-readable form.)

Appendix B ALMA Images and Radial Profiles

This appendix provides Band 6 ALMA images and radial profiles of the mm-wave emission in Figures 5 and 6, respectively.

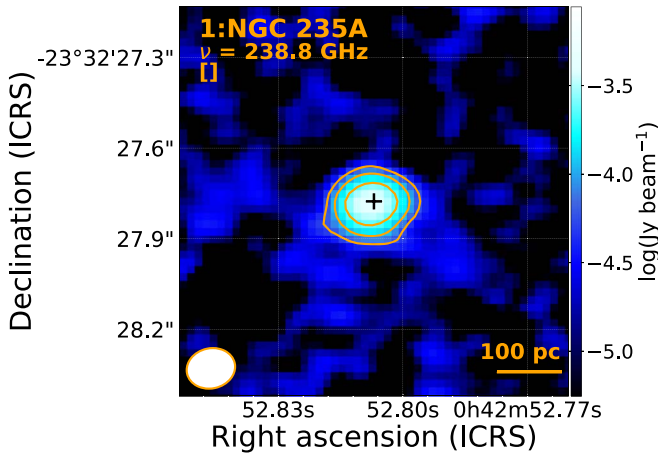


Figure 5. ALMA images, where north is up and east is to the left. In each figure, the beam size is indicated by the white ellipse at the bottom-left corner. The number to the left of the object name is the assigned number in this study and Paper I. The frequency is the rest-frame central frequency of the collapsed spectral window adopted, after removing any emission line flux. The central black cross indicates the peak of the nuclear mm-wave emission, expected to be the AGN position. If no mm-wave emission is detected, an unfilled diamond is shown where the AGN position is inferred either from Chandra or WISE observations. A morphological flag, which can consist of e and b, is also presented below the frequency. e and b indicate the presence of extended emission connected with the central unresolved component and the presence of isolated blob-like emission, respectively. Colors are assigned according to the flux density per beam following the color bar on the right side. The orange contours indicate where flux densities are $5\sigma_{\text{mm}}$, $10\sigma_{\text{mm}}$, $20\sigma_{\text{mm}}$, $40\sigma_{\text{mm}}$, $80\sigma_{\text{mm}}$, and $160\sigma_{\text{mm}}$, while dashed red ones are drawn where flux densities are $-5\sigma_{\text{mm}}$, if any. The individual values of σ_{mm} are listed in Table 3.

(The complete figure set (98 images) is available.)

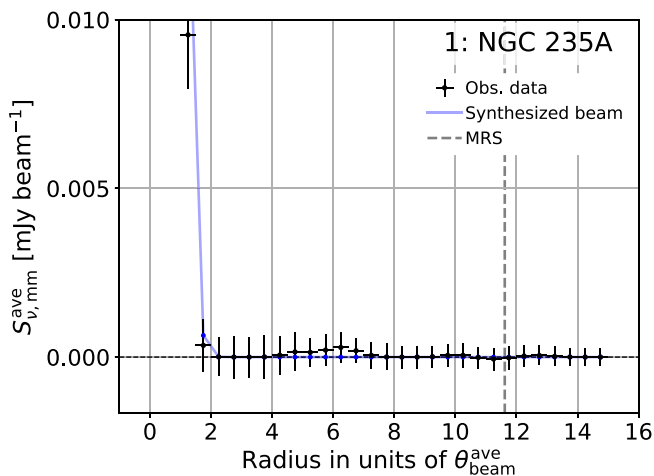


Figure 6. Radial surface brightness profiles. The radius is in units of the averaged beam size ($\theta_{\text{beam}}^{\text{ave}}$). In each figure, observed values are indicated by black error bars, but particularly those detected at significances more than three times the SEs with respect to an unresolved component are shown in orange. The blue line represents the profile of the synthesized beam whose innermost value is adjusted to the observed one. The dashed gray line indicates the MRS. (The complete figure set (98 images) is available.)

Appendix C Notes on Individual Objects

We present our discussions for the 28 individual objects that showed both or one of largely extended or blob-like components, as detailed in Section 4. For clarity of the discussions, we show the contour images of the targets in Figure 7.

C.1. 05: NGC 612

The ALMA image of this object was taken at a resolution of $0''.05$, revealing a patchy structure around the bright nuclear component within a radius of $0''.2$. Based on a Very Large Array (VLA) observation at 5 GHz, Ekers et al. (1978) reported an unresolved component whose diameter size was constrained to be $< 0''.3$. This resolution would be almost the highest ever achieved for this object, except for that of the ALMA observation, and thus there seem to be no data that help us to understand the patchy structure better.

C.2. 11: NGC 1068

Our 266 GHz image at a resolution of $\sim 0''.02$ shows diffuse emission around the nucleus (*a* in the corresponding panel of Figure 7; hereafter italic characters are used to indicate such components in the same way) and also three other diffuse components $\sim 0''.3$ away at a position angle (PA)⁴⁸ of $\sim 10^\circ$ (*b*), $\sim 0''.6$ away at a PA of $\sim 20^\circ$ (*c*), and $\sim 0''.2$ away at a PA of $\sim 180^\circ$ (*d*). A high-resolution continuum image obtained at almost the same resolution and frequency (i.e., $\approx 0''.02$ and 257 GHz) was presented by Impellizzeri et al. (2019). Their image revealed an X-shaped structure with a PA of $\sim 20^\circ$ (blue dotted arrow) around the nucleus, and they interpreted this as being due to edge brightening of a bicone-like ionized region. The X-shaped structure is clearly seen also in our image. Impellizzeri et al. (2019) measured the mm-wave and radio fluxes within a $0''.13$ square area with their ALMA data and VLA 43 GHz data, and then derived a spectral index of ~ 0.1 for the central emission. This is consistent with free-free emission ($\alpha_{\text{mm}} = 0.1$). However, based on an SED covering a wider range of ~ 1 –1000 GHz, Michiyama et al. (2023) presented two other possible scenarios: self-absorbed synchrotron emission from an area with a radius of ≈ 30 Schwarzschild radii and synchrotron emission from a jet.

The other diffuse component of *b* appears to be closely located in an area with bright emission found in the radio band (~ 1 –30 GHz). For example, a 1.4 GHz component, labeled C in Gallimore et al. (2004), was found at a resolution $\sim 0''.01$ (see also Gallimore et al. 1996; Muxlow et al. 1996). However, it is seen that the diffuse mm-wave emission (*b*) may be closer to the center by $\sim 0''.04$ (i.e., 2 pc) than the radio emission. Further investigation is crucial to confirm this and, if true, to understand this offset. Similarly, the components *c* and *d* virtually appear to coincide with the radio-bright northeast area and S2, reported in Gallimore et al. (2004). In their paper, it was suggested that the northeast emission might originate in an internal shock or denser jet plasma, and the S2 emission may be the result of a jet-driven shock.

In addition to the radio emission, IR emission at $12.5 \mu\text{m}$, for example, was mapped at a resolution of $0''.5$ within $\sim 1''$ by Bock et al. (2000). They revealed a structure that extends from the nucleus in the north and south directions. Apparently, no

⁴⁸ The PA is defined so that 0° is the north, and which increases counterclockwise.

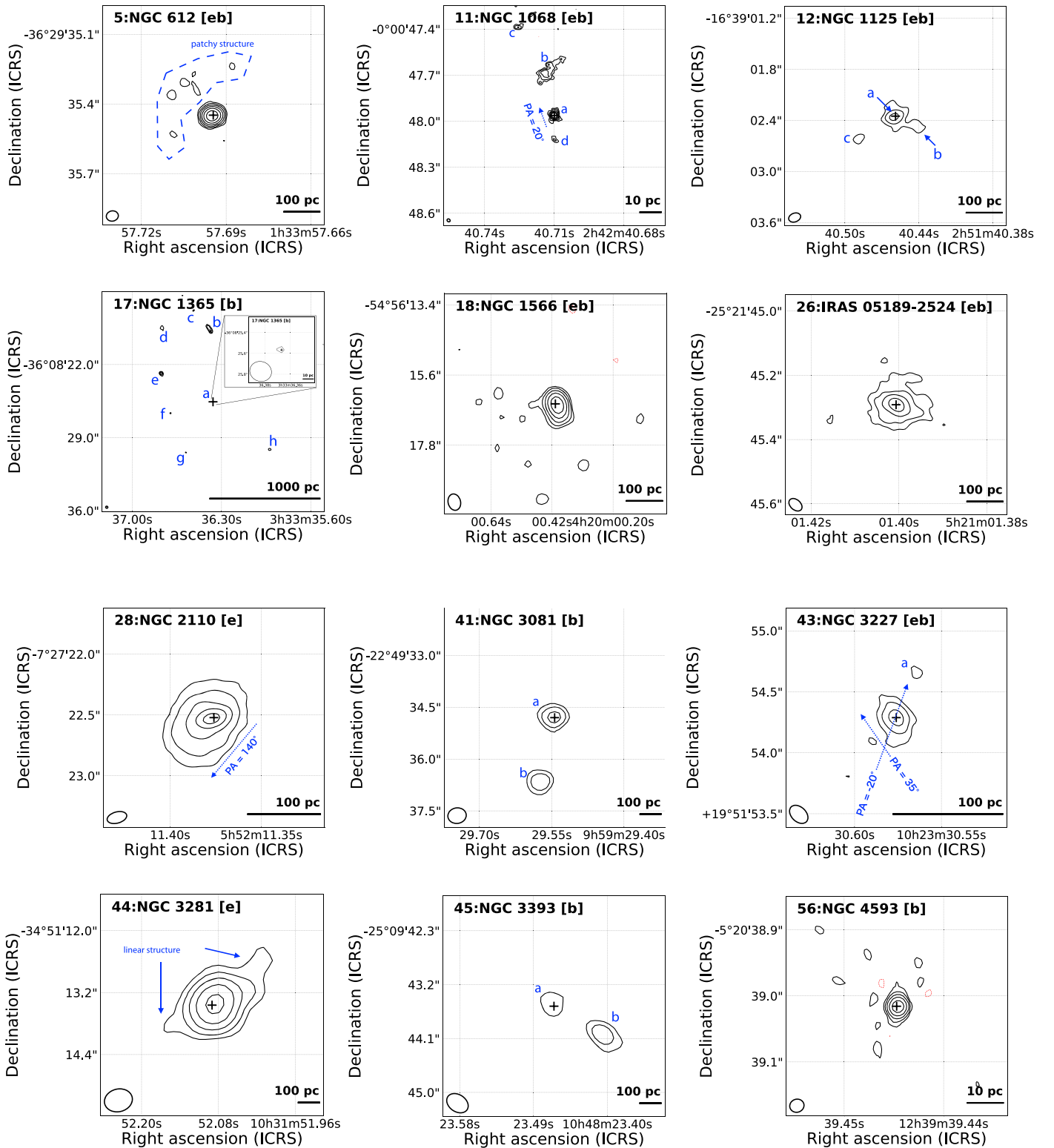


Figure 7. ALMA Band 6 images of the 28 objects that showed both or one of largely extended or blob-like components. North is up and east is to the left. Beam sizes are shown by the white ellipses in the bottom-left corners. Each central black cross indicates the peak of the nuclear mm-wave emission. Black solid contours indicate where flux densities per beam are $5\sigma_{\text{mm}}$, $10\sigma_{\text{mm}}$, $20\sigma_{\text{mm}}$, $40\sigma_{\text{mm}}$, $80\sigma_{\text{mm}}$, and $160\sigma_{\text{mm}}$, while red dotted ones are drawn where flux densities per beam are $-5\sigma_{\text{mm}}$. For three objects (NGC 5506, Mrk 520, and NGC 7172), flux densities per beam at $3\sigma_{\text{mm}}$ are indicated by black dotted contours. The individual values of σ_{mm} are listed in Table 3. The annotations in blue are used for the discussions in Appendix C.

peculiar MIR structures are associated with the structures *b*, *c*, and *d*.

Finally, we mention the secondary AGN recently suggested by Shin et al. (2021). The proposed area is $\sim 3''$ away from the

nucleus at a PA of $\sim 44^\circ$ (i.e., it thus lies outside the cutout of the image shown). No counterpart in the mm-wave band is however found. Given the very low X-ray luminosity of $\sim 10^{39}$ erg s^{-1} estimated by Shin et al. (2021), the

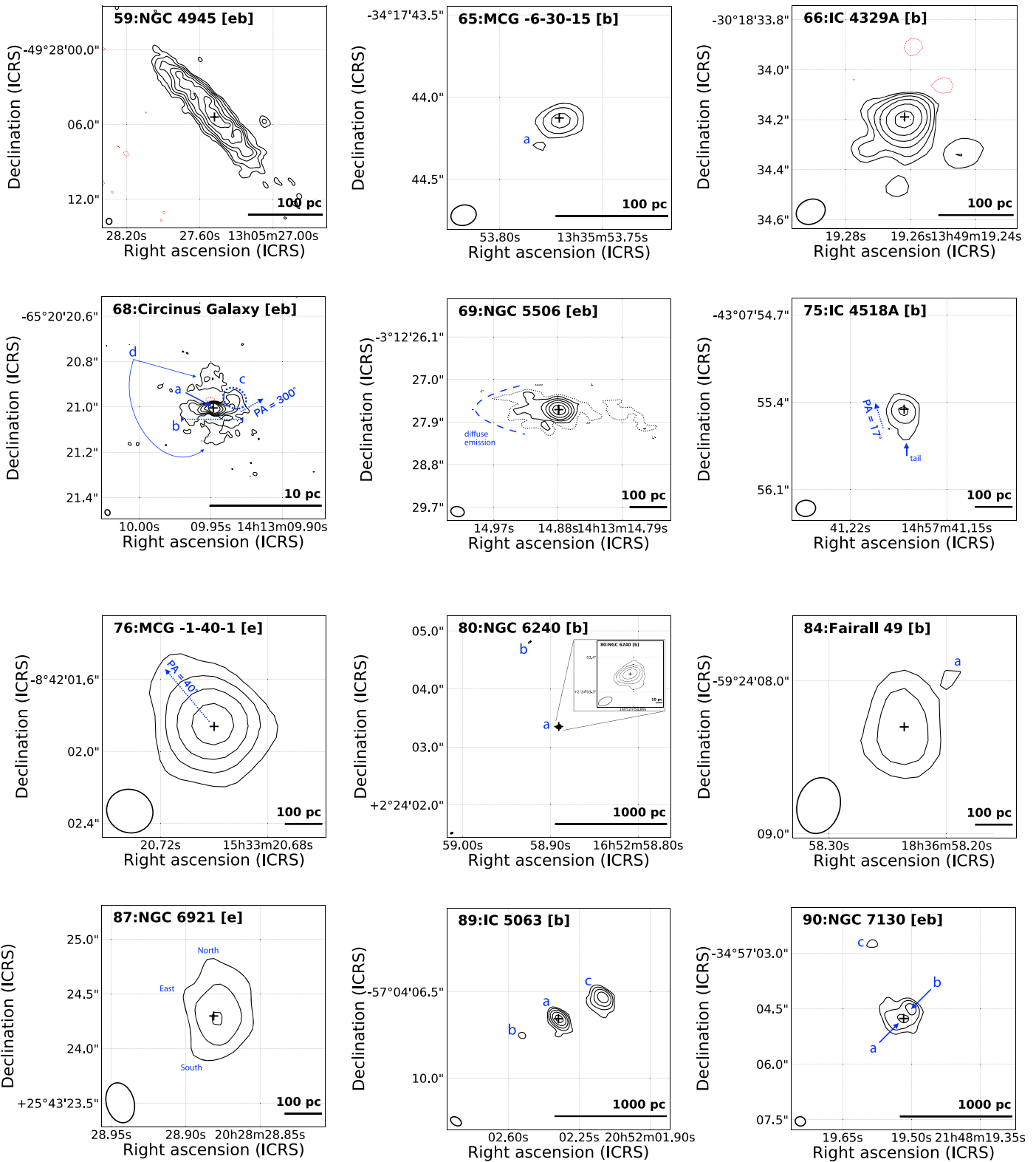


Figure 7. (Continued.)

nondetection may be natural. Our ALMA data have a sensitivity down to $\sim 10^{37}$ erg s $^{-1}$ in the mm-wave band, which can be converted to a 2–10 keV luminosity of $\sim 10^{41}$ erg s $^{-1}$ according to a relation presented in Paper I. Thus, the current data would be just insufficient to assess the presence of the suggested secondary AGN.

C.3. 12: NGC 1125

This source was observed at a resolution of $\approx 0''.1$ using ALMA and the image shows central core emission (*a*) and two nonnuclear components to the southwest and the southeast, labeled *b* and *c*, respectively. A moderate resolution ($\approx 0''.3$) image at 8.4 GHz was obtained with the VLA by Thean et al.

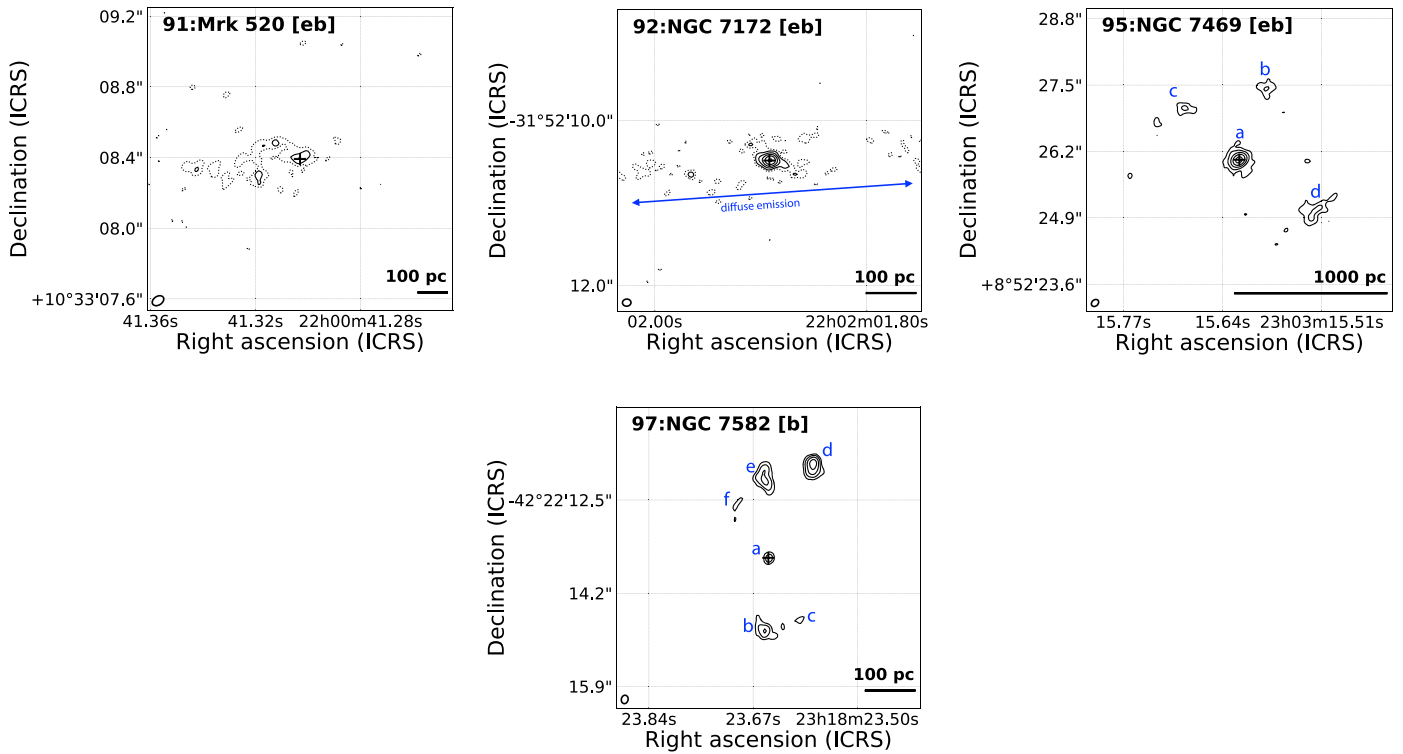


Figure 7. (Continued.)

(2000) and revealed a linear structure, which extends at a PA of 120° and has two peaks in the southeast and northwest regions, looking like radio lobes. The brightest radio component in the southeast direction appears to coincide with the mm-wave blob of *c*. No mm-wave counterpart is however found for the fainter northwest radio component. This could be because mm-wave emission is also fainter and thus cannot be detected at the achieved sensitivity. Regarding the component of *b*, no radio counterpart is found, perhaps due to the lower resolution of the radio image. Interestingly, the relative strength between the mm-wave and radio emission is highest in the center. This could suggest that the central and other lobe-like structures (*c* and maybe *b* as well) have different physical origins.

C.4. 17: NGC 1365

The image at a resolution of $\approx 0''.2$ shows seven significant components, labeled *b*, *c*, *d*, *e*, *f*, *g*, and *h* around the central component labeled *a*. Radio maps at different frequencies were presented in past studies (5 GHz–15 GHz; Sandqvist et al. 1982; Stevens et al. 1999; Thean et al. 2000; Sakamoto et al. 2007). At *a*, there appears to be a radio component according to a $\sim 1''$ resolution map created by Stevens et al. (1999). Furthermore, the five mm-wave components of *b*, *c*, *d*, *e*, and *f* appear to have radio counterparts that have been labeled D, E, G, H, and F, respectively, in previous studies (e.g., Sandqvist et al. 1982). Sakamoto et al. (2007) suggested that each of the D, E, G, and H regions possibly hosts a supercluster. Stevens et al. (1999) suggested that the components have moderate to steep spectral indices and are consistent with nonthermal emission. Regarding region F, the interpretation is not so clear, as discussed in Stevens et al. (1999). It is also currently unclear why the *g* and *h* components have no radio counterparts.

C.5. 18: NGC 1566

Complex mm-wave structures appear within a radius of $\sim 3''$. The central emission is slightly elongated to the north and is surrounded by several blob-like components. Combes et al. (2014) presented a submm-wave ALMA Band 7 image with a beam size of $0''.5$, comparable to our mm-wave data of $0''.4$. The authors argued that nonnuclear submm-wave emission exists and is from dust considering that the submm-wave emission follows a two-arm spiral structure detected in the CO($J=3-2$) line. Also, they estimated that the dust emission is likely to be stronger than synchrotron emission in the submm-wave band. However, our Band 6 continuum distribution appears to be different from the Band 7 one, suggesting that the Band 6 emission may have a different origin. Also, we mention the paper by Mezcuca et al. (2015), which presented $\approx 0''.1$ Hubble Space Telescope (HST) optical and VLT near-infrared (NIR) data including *K*-band emission and H₂ line emission. Apparently, none of the distributions seems to be spatially similar to the Band 6 structures. Eventually, nothing is found probably relevant to the extended and patchy components.

C.6. 26: IRAS 05189–2524

This is an ultraluminous IR galaxy and is considered to be in the final stage of a galaxy merger (e.g., Ricci et al. 2017c, 2021). Around the central peak emission, diffuse emission within a radius of $\sim 0''.1$ is revealed at a resolution of $0''.04$. The encompassing area contains emission of ~ 4 mJy, of which ≈ 1.3 mJy beam⁻¹ is ascribed to the peak emission. Thus, the contribution of the diffuse component is strong. Although there were few images taken at comparable resolutions, to our knowledge, NIR (2.2 and 3.8 μ m) images at resolutions of $0''.1-0''.2$ were obtained by Imanishi & Saito (2014), who utilized a camera of Subaru/IRCS in adaptive-optics mode.

The obtained NIR nuclear images seem to be overwhelmed by only a point source. Using shorter-wavelength ($\approx 1\text{--}2\ \mu\text{m}$) HST/NICMOS data at similar resolutions of $0''.1\text{--}0''.2$, Scoville et al. (2000) also reported an unresolved component, but additionally mentioned the possible presence of low-level extended emission. To discuss more about whether the mm-wave diffuse emission has an NIR counterpart, higher-resolution images with better sensitivities are desired.

C.7. 28: NGC 2110

A core-like component appears to be surrounded by a halo, whose major axis is oriented at a PA of $\sim 140^\circ$. In the adjacent cm-wave band, a jet in a north–south direction was clearly revealed up to $4''$ on each side (e.g., Ulvestad & Wilson 1983). The difference in angle between the radio jet and the mm-wave halo would suggest that the mm-wave emission would not be dominated by the jet. Instead, ionization cones traced by optical ionization lines (e.g., [O III] and [S II]+H α) have similar angles to that of the halo (e.g., Mulchaey et al. 1994). Spatially resolved X-ray iron emission that could be due to X-ray irradiation of gas by the AGN also has a similar angle (Kawamuro et al. 2020, 2021). Thus, the mm-wave halo could be more relevant to the AGN photoionization process than the cm-wave jet.

C.8. 41: NGC 3081

In addition to the central nuclear emission with $\sim 0.7\ \text{mJy beam}^{-1}$ (a), our image at a resolution of $\sim 0''.5$ unveils a comparably bright component (b) with $\sim 0.5\ \text{mJy beam}^{-1}$ $\sim 2''$ away from the nucleus in the south. An 8.4 GHz image was obtained at a similar beam size of $\sim 0''.4$ by Mundell et al. (2009) using the VLA, and shows radio emission ($\sim 1\ \text{mJy}$) spatially consistent with a . On the other hand, there is no significant radio emission around the south mm-wave component (b). The upper limit of the radio emission, corresponding to $3 \times \text{rms}$, is estimated to be $\sim 0.05\ \text{mJy beam}^{-1}$, leading to an upper limit of < -0.7 for the spectral index. This is smaller than that for the central emission (~ 0.7). As an insight from different wavelength data, Ma et al. (2021) spatially revealed ionized gas at resolutions below $0''.1$. According to optical emission line diagnostics with the [N II]/H α and [O III]/H β , AGN-like or LINER-like optical emission line ratios were found around b . Thus, the mm-wave emission in b may be due to the AGN.

C.9. 43: NGC 3227

Millimeter-wave continuum emission in the central $1'' \times 1''$ region of the object was discussed in detail by Alonso-Herrero et al. (2019), who used the same ALMA data as we used. Here, we give a brief summary of their discussion, and those who are interested in more details should check Alonso-Herrero et al. (2019) and references therein.

The authors suggested that there exist two mm-wave components with different PAs of $\sim 35^\circ$ and $\sim -20^\circ$, indicated in Figure 7. The centrally concentrated component with a PA $\sim 35^\circ$ may be relevant to an ionization cone and a radio jet. Using HST observations of [N II] and H α , an ionization cone was mapped at a similar PA. The presence of a jet in the same direction, or synchrotron emission, was inferred from a spectral-index map that Alonso-Herrero et al. (2019) made by

combining mm-wave data with additional submm-wave ALMA data.

The other component at PA $\sim -20^\circ$ (a) is located $0''.5$ away from the nuclear peak, and the angle almost aligns with the axis of a nuclear disk. mm-wave to submm-wave spectral indices therein were found to be consistent with thermal processes and free–free emission. While considering this fact and other multiwavelength data (e.g., Br γ), Alonso-Herrero et al. (2019) discussed that SF may contribute to the mm-wave emission. In the direction of the mm-wave component, cm-wave radio emission was also revealed by Mundell et al. (1995) and could originate from supernova remnants in the above context.

C.10. 44: NGC 3281

A northwest–southeast linear structure, parallel to a PA of $\sim 100^\circ\text{--}130^\circ$, can be seen. In contrast, Schmitt et al. (2001) reported only unresolved radio (8.46 GHz) emission with a size upper limit of $< 60\ \text{pc}$ based on a spatial resolution of $\sim 0''.2$. This is better than that achieved by the ALMA observation ($0''.5$). As a spatially extended signature of AGN activity, a narrow-line region was mapped by using optical [O III] emission in Schmitt et al. (2003), and this extends toward the northeast. Eventually, from the radio and optical observations, we cannot find mm-wave counterparts. Instead, it seems that the major axis of the galaxy disk has a similar angle of $\sim 130^\circ$ (Schmitt et al. 2003). Thus, the linear structure could be associated with gas, or SF processes, distributed in the galaxy disk.

C.11. 45: NGC 3393

This object is known to have three radio spots in the northwest, nuclear, and southwest areas (e.g., Cooke et al. 2000; Koss et al. 2015; Maksym et al. 2017; Finlez et al. 2018), and our ALMA image at a resolution of $0''.3$ shows two significant components: a in the nucleus and b in the southwest direction. Thus, mm-wave emission spatially corresponding to the northeast radio spot is undetected. At a similar resolution of $\sim 0''.2$, Schmitt et al. (2001) estimated the 8.5 GHz flux densities for the southwest, nuclear, and northeast components to be $\sim 1\ \text{mJy}$, $\sim 1\ \text{mJy}$, and $\sim 8\ \text{mJy}$, respectively. On the other hand, their mm-wave flux densities per beam are $\lesssim 0.1\ \text{mJy beam}^{-1}$ ($5\sigma_{\text{mm}}$ upper limit), $\sim 0.2\ \text{mJy beam}^{-1}$, and $\sim 0.4\ \text{mJy beam}^{-1}$, respectively. If the southwest and northeast radio components have similar spectral indices of 0.7–0.9, as inferred from the study of Morganti et al. (1999), the nondetection of the northeast component in the ALMA image is reasonable. In contrast, the nuclear component looks relatively bright compared with the southwest one (i.e., a higher ratio of mm-wave and radio flux densities). Indeed, the nuclear emission may have a spectral index of ~ 0.5 according to the 8.5 GHz and 229 GHz flux densities. This may suggest different physical origins for the central and other components.

According to Maksym et al. (2019), a radio jet drives a shock that produces the X-ray emission and optical [O III] emission. Moreover, the authors suggested that the shocked gas has enough energy to evacuate gas from the galaxy. Thus, the mm-wave emission (b) may also be tracing such a phenomenon, suggesting that mm-wave observations can be a tool for unveiling such shocked regions.

We note that Fabbiano et al. (2011) suggested the presence of another AGN in the southeast region. No significant

emission is, however, found around that position in our ALMA image.

C.12. 56: NGC 4593

In addition to the central core emission, a north–south component appears to extend up to $0''.03$ on each side, and also there exist blob-like components. Data publicly presented to date seem to have achieved resolutions of $\sim 0''.2$ at best (e.g., Thean et al. 2000; Schmitt et al. 2001; Fischer et al. 2021). Thus, we cannot discuss the origin with the help of the other data.

C.13. 59: NGC 4945

Bright mm-wave emission is seen across the galaxy disk in the northeast–southwest direction. The flux density for the disk that we define as a $3'' \times 14''$ rectangular region with a PA of 43° is ~ 600 mJy, and its intraband spectral index is constrained to be -2.1 ± 0.2 . These are largely different from those at the central peak (*a*) of $S_{\nu, \text{mm}}^{\text{peak}} \sim 40$ mJy beam $^{-1}$ and $\alpha_{\text{mm}} = -0.4 \pm 0.2$, indicating that the significant component is different between the central peak and the disk region. An SED in the 5–350 GHz band was analyzed by Bendo et al. (2016) with a focus on the central disk region within $12'' \times 30''$ (see also Henkel et al. 2018), and the 230 GHz continuum flux of 1.3 Jy was basically reproduced by combining thermal dust emission and free–free emission, resulting in an index of ~ -3 . This index may be expected in our data as well, but is different from our constraint of -2.1 ± 0.2 . This could be because thermal dust grains are more broadly distributed than free–free-emitting photoionized gas, as mentioned by Bendo et al. (2016), and the mm-wave slope is flattened in our high-resolution data where dust emission with a steep slope ($\alpha_{\text{mm}} = -4$ to -3) is relatively missed.

C.14. 65: MCG–6–30–15

At a PA of $\approx 140^\circ$ – 150° , a blob-like component (*a*) is revealed at a resolution of $\sim 0''.1$. Radio observations at 8 GHz and 1.5 GHz were performed (Nagar et al. 1999), but the resolutions were much coarser (a few arcseconds), and detected radio components were not spatially resolved. HST images were reported in some works (Ferrarese & Merritt 2000; Schmitt et al. 2003), and show that the host galaxy and also a narrow-line region traced by the optical [O III] emission have similar PAs of -65° , slightly different from the PA of the mm-wave component. Thus, the origin could be due neither to phenomena in the main body of the host galaxy nor to the AGN, and currently the origin is unclear.

C.15. 66: IC 4329A

In our image at a resolution of $0''.1$, nuclear emission is prominent, and patchy components are seen. Radio (8.4 GHz) emission was imaged with a beam of $0''.3 \times 0''.7$ by Thean et al. (2000) and significant radio emission with 4.9 mJy beam $^{-1}$ exists around the nuclear mm-wave emission. However, for further discussion, as the radio image is very noisy, better radio images with higher sensitivities and also higher spatial resolutions are desired to be compared with the ALMA one.

C.16. 68: Circinus Galaxy

Around the bright nuclear core (*a*), extended emission in the east–west direction (*b*) exists on a scale of a few parsecs. In addition, there appear to be two components: one located to the northwest (*c*) and the symmetrically distributed structure from north to south (*d*). In an area within a radius of $0''.35$ which includes all the above structures, the flux density is ~ 30 mJy. Since the peak flux density per beam is ~ 15 mJy beam $^{-1}$, an important fraction of the mm-wave emission within the area is resolved at our resolution of ~ 0.5 pc.

Submm-wave ALMA Band 7 continuum emission was imaged at a resolution of $\sim 0''.3$ by Izumi et al. (2018). The resolution is coarser than achieved with our data (i.e., $0''.02$), thus hampering a visual comparison with our image. However, the authors reported the presence of an elongated structure on a scale of $0''.05$ (~ 1 pc) at a PA of $\sim 300^\circ$ (blue dotted arrow) based on visibility modeling. They suggested that this would trace the polar dust structure found by MIR observations (Tristram et al. 2014). Component *c* appears to coincide with that, thus perhaps indicating dust emission as the origin of *c*. The more prominent east–west emission of *b* could have a different origin, however, given its direction, and currently, it is unclear what its origin is. Finally, the origin of component *d* is also unclear due to the lack of meaningful data available. Each of the north and south components spreads on a scale of $1''$ and has a flux density of ~ 0.9 mJy. To determine the physical mechanism for each component, it is important to determine the index, but our ALMA data are not sufficient to constrain it well. Thus, additional data at adjacent different wavelengths or those obtained at higher sensitivities are desired.

C.17. 69: NGC 5506

At a $\approx 0''.2$ resolution, in addition to the bright central emission, diffuse emission is seen, particularly in the east direction, while there may be a west component as well. Exceptionally, dotted contours at $3\sigma_{\text{mm}}$, which are formally insignificant but could be real, are presented. Orienti & Prieto (2010) presented three maps at 4.8 GHz, 8.4 GHz, and 14.9 GHz by analyzing VLA data, whose resolutions are $\sim 0''.4$, $0''.2$, and $0''.6$, respectively. Interestingly, while diffuse halo structures were revealed at the two lowest frequencies within a radius of $\sim 2''$, the 14.9 GHz map shows that a component, extending to the east and west directions by $\sim 2''$ on each side, is prominent. Its physical origin was not discussed in the paper. The 14.9 GHz structure looks similar to the mm-wave one at least in the east, although it is slightly tilted counterclockwise by $\sim 20^\circ$ – 40° . This suggests their association. Furthermore, given that the PAs of the 14.9 GHz and mm-wave components are similar to that of the galaxy disk, they may be related to gas in the galaxy disk. Probably, a higher inclination angle (i.e., edge-on view) to NGC 5506, where line-of-sight column densities of gas can be higher, would make it easier to identify emission relevant to the gas in the galaxy disk.

C.18. 75: IC 4518A

This is a member of a merging system with IC 4518B. The prominent core emission, which appears to have a tail-like structure with a PA of 200° – 210° , is seen in our data at $\approx 0''.2$ resolution. To our knowledge, no high-resolution radio images have been published, while Condon et al. (1996) showed a 1.4

GHz image at a resolution $\sim 10''$. As data taken at comparable resolutions, Asmus (2019) showed 12 μm and 18 μm images at resolutions of $\sim 0''.4\text{--}0''.5$. The author revealed an elongated MIR component with a PA of 17° (blue dotted arrow), which is almost parallel to the mm-wave tail. Given the argument by Asmus (2019) that such an MIR component is due to dusty wind by an AGN, the mm-wave tail could be also driven by the AGN. As a different supportive result for the AGN-driven emission, Díaz-Santos et al. (2010) found extended [S IV] 10.51 μm line emission out to $\sim 0''.8$ to the south direction, and interpreted this as a sign of the presence of a narrow-line region, consistent with the AGN origin.

C.19. 76: MCG-1-40-1

In addition to the central core-like emission, our high-resolution image created by a beam of $0''.26 \times 0''.24$ revealed a horn-like structure at a PA of $\sim 40^\circ$. However, as no meaningful data taken at comparable resolutions are available, discussion on its origin is currently difficult.

C.20. 80: NGC 6240

This is a well-studied merging system, and two active nuclei have been identified at various wavelengths (e.g., Komossa et al. 2003; Gallimore & Beswick 2004; Gallimore et al. 2004; Puccetti et al. 2016). According to the recent study by Kollatschny et al. (2020), there may be another inactive nucleus to the south of the active nucleus in the south. Our image at $0''.03$ resolution shows two mm-wave compact components: one at the center (*a*) and the other in the north (*b*), probably associated with the first and second active nuclei (e.g., Gallimore et al. 2004). On the other hand, insignificant emission is found around the third nucleus (*c*), as already confirmed by Treister et al. (2020), who analyzed the same ALMA data. Medling et al. (2019) suggested that within a radius of $0''.077$ around each of the two active nuclei, thermal dust emission is dominant at 242 GHz. This argument was based on the result that the extrapolated mm-wave flux densities from 5 GHz ones by adopting a spectral index of ≈ 1 are lower than observed. In contrast, our higher-resolution data suggest a spectral index of $\alpha_{\text{mm}} \sim 1.0 \pm 0.4$ for the nucleus (*a*), inconsistent with the dominance of thermal emission. Regarding the north nucleus (*b*), the spectral index is not constrained, as its mm-wave emission is not detected in individual spectral windows.

We comment on the relation of the mm-wave and X-ray luminosities for the two active nuclei. In Paper I, we added their luminosities together to be consistent with the X-ray flux derived in Ricci et al. (2017c), but we also confirm that the two nuclei follow a mm-wave-to-X-ray regression line (Table 1 in Paper I) within 2σ , even if we consider them separately. The used X-ray luminosities are taken from Puccetti et al. (2016), who derived intrinsic 2–10 keV luminosity for each using NuSTAR, Chandra, XMM-Newton, and BeppoSAX data.

C.21. 84: Fairall 49

Our ALMA image at a resolution of $0''.3$ shows an isolated signal at a PA of -50 to -40° (*a*). According to a subarcsecond MIR observation by Asmus et al. (2016), an extended MIR component possibly exists, and its PA was constrained to be 42° (see also Isbell et al. 2021). The PA does not seem to indicate that the mm-wave signal is associated with

the MIR component. Instead, the host galaxy has a PA of 120° and thus seems aligned to the signal. To discuss further whether a host-galaxy phenomenon is indeed relevant, detailed analyses of host-galaxy images are necessary.

C.22. 87: NGC 6921

Three horn-like structures in the north, east, and south directions are seen in our mm-wave image constructed with a beam of $0''.37 \times 0''.25$. Images at comparable resolutions are not found. Additional observations are desired for discussing the nonnuclear components.

C.23. 89: IC 5063

Our ALMA image produced at $\approx 0''.4$ resolution shows three compact components: one at the central AGN position (*a*) and the other two to the southeast and northwest (*b* and *c*). They are almost linearly aligned at an angle of $\sim 115^\circ$, which is similar to that found for linear structures at frequencies of $\sim 10\text{--}20$ GHz. The mm-wave components were already discussed by Morganti et al. (2015) with a different ALMA data set at ~ 230 GHz. Using 17 GHz radio data from Morganti et al. (2007), the authors constrained the spectral indices for the southeast, northwest, and central components to be 0.87 ± 0.02 , 0.93 ± 0.01 , and 0.33 ± 0.01 , respectively. The resolutions of the used 17 and 230 GHz data were $\sim 0''.4\text{--}0''.5$, comparable to ours. The indices favor nonthermal processes as the origin of the mm-wave components, and moreover the flatter slope of the central component could suggest that its origin is different from those of the southeast and northwest ones.

We moreover note that IC 5063 exhibits extended X-ray emission along the mm-wave and radio structures (Gómez-Guijarro et al. 2017). Recently, Travascio et al. (2021) performed a spatially resolved X-ray spectral analysis using Chandra and suggested that extended X-ray emission in the soft X-ray band (< 3 keV) can be reproduced by either two photoionized gas models or a sum of photoionized and collisionally ionized gas models. Furthermore, hard-X-ray Fe XXV emission was detected at the northwest radio structure. On the basis of these facts, the authors suggested that the X-ray emission may be caused by interaction of a radio jet with the interstellar medium. Thus, the mm-wave emission seems to also trace the interaction regions.

C.24. 90: NGC 7130

Our mm-wave image at a resolution of $\approx 0''.3$ reveals two bright nuclear peaks (*a* and *b*). In addition, to the north, a compact component (*c*) is seen. Zhao et al. (2016) studied this object using not only ALMA Band 9 data at a similar resolution of $\approx 0''.2$, who observed CO($J = 6\text{--}5$), but also other supplementary data at different wavelengths (e.g., optical and radio bands). They found a radio core near the southeast nucleus (*a*) using VLA 8.4 GHz continuum data provided in Thean et al. (2000), and also a higher 8.4 GHz-to-CO ($J = 6\text{--}5$) luminosity ratio than expected for SF regions therein. These support that an AGN is located at the southeast position of *a*. We note that *a* is consistent with a peak of optical emission therein (González Delgado et al. 1998). Following the analysis and suggestion of Zhao et al. (2016), we defined the southeast nucleus (*a*) as an AGN position. On the other hand, Zhao et al. (2016) did not suggest the presence of an AGN in the

northwest region (*b*), due to the absence of compact radio emission and a SF-region-like radio-to-CO ($J = 6-5$) ratio in the area. We note that we created a high-resolution Chandra image ($\approx 0''.1$) in the 3–7 keV band, probably tracing AGN emission (Levenson et al. 2005), and we did not find clear double nuclei.

Lastly, we mention that the Band 9 emission around the north mm-wave component (*c*) was attributed to dust emission by Zhao et al. (2016). The peak emission is $\approx 10-20$ mJy beam $^{-1}$, and if a thermal component with $\alpha_{\text{mm}} = -3.5$ is dominant, the predicted flux at 262 GHz (our mm-wave frequency) is ~ 0.5 mJy beam $^{-1}$. This is consistent with our observed value of 0.5 mJy beam $^{-1}$, suggesting that the Band 6 emission would also be dust emission.

C.25. 91: Mrk 520

Our mm-wave image at a high resolution of $0''.06$, corresponding to ~ 30 pc for the object, shows that overall the morphology looks diffuse. This can be noticed more clearly by considering fainter emission at $3\sigma_{\text{mm}}$ (dotted lines) additionally. A 5 GHz image was presented at a much coarser resolution of $\sim 1''.4$ by Lonsdale et al. (1992), and the radio emission has a core-like morphology. This radio emission seems to coincide with the peak of the mm-wave image. However, to confirm whether most of the radio emission is indeed associated with the mm-wave peak or appears like the diffuse mm-wave emission, it is important to obtain a higher-resolution radio image.

C.26. 92: NGC 7172

In addition to the central core emission, diffuse emission in the east–west direction appears at $3\sigma_{\text{mm}}$, although this is formally insignificant. The morphology appears to trace the galaxy disk (e.g., Malkan et al. 1998). Therefore the diffuse emission would trace gas in the disk, or SF regions. As in NGC 5506 (Appendix C.17), the edge-on view to NGC 7172 would enable us to identify that emission. We note that a possible radio counterpart for the core was found with a $0''.4$ beam in Thean et al. (2000).

C.27. 95: NGC 7469

Around the strongest central component (*a*), there are three blobs (*b*, *c*, and *d*). These are likely to be encompassed by an annular starburst ring with radii of $\sim 1''.5-2''.5$ found at different wavelengths (e.g., Soifer et al. 2003; Díaz-Santos et al. 2007; Orienti & Prieto 2010), and are spatially coincident with significant 349.7 GHz components presented at $\approx 0''.50 \times 0''.40$ resolution by Izumi et al. (2015). At that 350 GHz band, the three components have flux densities per beam of $\approx 1.0-1.7$ mJy beam $^{-1}$ (Izumi et al. 2015). With Band 6 ALMA data, different from ours, Imanishi et al. (2016) also measured their flux densities at $\sim 260-266$ GHz with a similar beam size of $0''.57 \times 0''.52$. By correcting for the slight difference in beam size, the spectral slopes between the two bands are estimated to be ≈ -2.6 . This suggests that thermal emission with $\alpha_{\text{mm}} \sim -3.5$ may not be the only component. We note that, in our mm-wave data, the three components were not detected in a sufficient number of windows to derive the spectral index.

C.28. 97: NGC 7582

Our mm-wave image reveals nuclear emission (*a*) and also five surrounding components labeled *b*, *c*, *d*, *e*, and *f*. Hints on the origins can be obtained by comparing the ALMA image with the MIR [Ne II] emission line image of Wold & Galliano (2006). The MIR image revealed six areas with bright MIR emission, labeled M1, M2, M3, M4, M5, and M6. The mm-wave components of *b*, *c*, *d*, *e*, and *f* appear to coincide with M1, M2, M3+M4, M5, and M6, respectively. The authors described that the six MIR structures may be due to young star clusters embedded in dust and, otherwise, to clusters that are older and obscured by a screen of dust. However, the recent study by Ricci et al. (2018) suggested that AGN-driven jets/winds could be related to the MIR structures, based on their associations with NIR emission lines (i.e., [Fe II] and Br γ), while the contributions of young stellar clusters were not completely excluded. Thus, the mm-wave components may originate from AGN jets/winds.

ORCID iDs

Taiki Kawamuro  <https://orcid.org/0000-0002-6808-2052>
 Claudio Ricci  <https://orcid.org/0000-0001-5231-2645>
 Richard F. Mushotzky  <https://orcid.org/0000-0002-7962-5446>
 Masatoshi Imanishi  <https://orcid.org/0000-0001-6186-8792>
 Franz E. Bauer  <https://orcid.org/0000-0002-8686-8737>
 Federica Ricci  <https://orcid.org/0000-0001-5742-5980>
 Michael J. Koss  <https://orcid.org/0000-0002-7998-9581>
 George C. Privon  <https://orcid.org/0000-0003-3474-1125>
 Benny Trakhtenbrot  <https://orcid.org/0000-0002-3683-7297>
 Takuma Izumi  <https://orcid.org/0000-0001-9452-0813>
 Kohei Ichikawa  <https://orcid.org/0000-0002-4377-903X>
 Alejandra F. Rojas  <https://orcid.org/0000-0003-0006-8681>
 Krista Lynne Smith  <https://orcid.org/0000-0001-5785-7038>
 Taro Shimizu  <https://orcid.org/0000-0002-2125-4670>
 Kyuseok Oh  <https://orcid.org/0000-0002-5037-951X>
 Jakob S. den Brok  <https://orcid.org/0000-0002-8760-6157>
 Shunsuke Baba  <https://orcid.org/0000-0002-9850-6290>
 Mislav Baloković  <https://orcid.org/0000-0003-0476-6647>
 Chin-Shin Chang  <https://orcid.org/0000-0001-9910-3234>
 Darshan Kakkad  <https://orcid.org/0000-0002-2603-2639>
 Ryan W. Pfeifle  <https://orcid.org/0000-0001-8640-8522>
 Matthew J. Temple  <https://orcid.org/0000-0001-8433-550X>
 Yoshihiro Ueda  <https://orcid.org/0000-0001-7821-6715>
 Fiona Harrison  <https://orcid.org/0000-0002-4226-8959>
 Meredith C. Powell  <https://orcid.org/0000-0003-2284-8603>
 Daniel Stern  <https://orcid.org/0000-0003-2686-9241>
 Meg Urry  <https://orcid.org/0000-0002-0745-9792>
 David B. Sanders  <https://orcid.org/0000-0002-1233-9998>

References

- Alonso-Herrero, A., García-Burillo, S., Pereira-Santaella, M., et al. 2019, *A&A*, 628, A65
 Asmus, D. 2019, *MNRAS*, 489, 2177
 Asmus, D., Hönig, S. F., & Gandhi, P. 2016, *ApJ*, 822, 109
 Baloković, M., Harrison, F. A., Madejski, G., et al. 2020, *ApJ*, 905, 41
 Baumgartner, W. H., Tueller, J., Markwardt, C. B., et al. 2013, *ApJS*, 207, 19
 Behar, E., Baldi, R. D., Laor, A., et al. 2015, *MNRAS*, 451, 517
 Behar, E., Vogel, S., Baldi, R. D., Smith, K. L., & Mushotzky, R. F. 2018, *MNRAS*, 478, 399
 Bendo, G. J., Henkel, C., D’Cruze, M. J., et al. 2016, *MNRAS*, 463, 252
 Bock, J. J., Neugebauer, G., Matthews, K., et al. 2000, *AJ*, 120, 2904

- Burlon, D., Ajello, M., Greiner, J., et al. 2011, *ApJ*, **728**, 58
- Chiaraluce, E., Panessa, F., Bruni, G., et al. 2020, *MNRAS*, **495**, 3943
- Combes, F., García-Burillo, S., Casasola, V., et al. 2014, *A&A*, **565**, A97
- Condon, J. J. 1992, *ARA&A*, **30**, 575
- Condon, J. J., Helou, G., Sanders, D. B., & Soifer, B. T. 1996, *ApJS*, **103**, 81
- Cooke, A. J., Baldwin, J. A., Ferland, G. J., Netzer, H., & Wilson, A. S. 2000, *ApJS*, **129**, 517
- Courtois, H. M., Tully, R. B., Hoffman, Y., et al. 2017, *ApJL*, **847**, L6
- Díaz-Santos, T., Alonso-Herrero, A., Colina, L., et al. 2010, *ApJ*, **711**, 328
- Díaz-Santos, T., Alonso-Herrero, A., Colina, L., Ryder, S. D., & Knapen, J. H. 2007, *ApJ*, **661**, 149
- Ekers, R. D., Goss, W. M., Kotanyi, C. G., & Skellern, D. J. 1978, *A&A*, **69**, L21
- Elvis, M., Wilkes, B. J., McDowell, J. C., et al. 1994, *ApJS*, **95**, 1
- Fabbiano, G., Wang, J., Elvis, M., & Risaliti, G. 2011, *Natur*, **477**, 431
- Ferrarese, L., & Merritt, D. 2000, *ApJL*, **539**, L9
- Finlez, C., Nagar, N. M., Storchi-Bergmann, T., et al. 2018, *MNRAS*, **479**, 3892
- Fischer, T. C., Secrest, N. J., Johnson, M. C., et al. 2021, *ApJ*, **906**, 88
- Francis, L., Johnstone, D., Herczeg, G., Hunter, T. R., & Harsono, D. 2020, *AJ*, **160**, 270
- Gallimore, J. F., Baum, S. A., & O'Dea, C. P. 2004, *ApJ*, **613**, 794
- Gallimore, J. F., Baum, S. A., O'Dea, C. P., & Pedlar, A. 1996, *ApJ*, **458**, 136
- Gallimore, J. F., & Beswick, R. 2004, *AJ*, **127**, 239
- Gandhi, P., Horst, H., Smette, A., et al. 2009, *A&A*, **502**, 457
- García-Burillo, S., Alonso-Herrero, A., Ramos Almeida, C., et al. 2021, *A&A*, **652**, A98
- Gómez-Guijarro, C., González-Martín, O., Ramos Almeida, C., Rodríguez-Espinosa, J. M., & Gallego, J. 2017, *MNRAS*, **469**, 2720
- González Delgado, R. M., Heckman, T., Leitherer, C., et al. 1998, *ApJ*, **505**, 174
- Henkel, C., Mühle, S., Bendo, G., et al. 2018, *A&A*, **615**, A155
- Hickox, R. C., & Alexander, D. M. 2018, *ARA&A*, **56**, 625
- Ho, L. C. 2008, *ARA&A*, **46**, 475
- Imanishi, M., Nakanishi, K., & Izumi, T. 2016, *AJ*, **152**, 218
- Imanishi, M., & Saito, Y. 2014, *ApJ*, **780**, 106
- Impellizzeri, C. M. V., Gallimore, J. F., Baum, S. A., et al. 2019, *ApJL*, **884**, L28
- Inoue, Y., & Doi, A. 2018, *ApJ*, **869**, 114
- Inoue, Y., Khangulyan, D., & Doi, A. 2020, *ApJL*, **891**, L33
- Isbell, J. W., Burtscher, L., Asmus, D., et al. 2021, *ApJ*, **910**, 104
- Izumi, T., Kohno, K., Aalto, S., et al. 2015, *ApJ*, **811**, 39
- Izumi, T., Wada, K., Fukushige, R., Hamamura, S., & Kohno, K. 2018, *ApJ*, **867**, 48
- Kawamuro, T., Izumi, T., Onishi, K., et al. 2020, *ApJ*, **895**, 135
- Kawamuro, T., Ricci, C., Imanishi, M., et al. 2022, arXiv:2208.03880
- Kawamuro, T., Ricci, C., Izumi, T., et al. 2021, arXiv:2109.09742
- Kawamuro, T., Ueda, Y., Tazaki, F., Ricci, C., & Terashima, Y. 2016a, *ApJS*, **225**, 14
- Kawamuro, T., Ueda, Y., Tazaki, F., Terashima, Y., & Mushotzky, R. 2016b, *ApJ*, **831**, 37
- Kawamuro, T., Ueda, Y., Tazaki, F., & Terashima, Y. 2013, *ApJ*, **770**, 157
- Kollatschny, W., Weilbacher, P. M., Ochmann, M. W., et al. 2020, *A&A*, **633**, A79
- Komossa, S., Burwitz, V., Hasinger, G., et al. 2003, *ApJL*, **582**, L15
- Koss, M. J., Blecha, L., Bernhard, P., et al. 2018, *Natur*, **563**, 214
- Koss, M. J., Ricci, C., Trakhtenbrot, B., et al. 2022a, *ApJS*, **261**, 2
- Koss, M. J., Trakhtenbrot, B., Ricci, C., et al. 2022b, *ApJS*, **261**, 1
- Koss, M. J., Romero-Cañizales, C., Baronchelli, L., et al. 2015, *ApJ*, **807**, 149
- Laor, A., & Behar, E. 2008, *MNRAS*, **390**, 847
- Levenson, N. A., Weaver, K. A., Heckman, T. M., Awaki, H., & Terashima, Y. 2005, *ApJ*, **618**, 167
- Lonsdale, C. J., Lonsdale, C. J., & Smith, H. E. 1992, *ApJ*, **391**, 629
- Ma, J., Maksym, W. P., Fabbiano, G., et al. 2021, *ApJ*, **908**, 155
- Mainzer, A., Bauer, J., Grav, T., et al. 2011, *ApJ*, **731**, 53
- Makarov, D., Prugniel, P., Terekhova, N., Courtois, H., & Vauglin, I. 2014, *A&A*, **570**, A13
- Maksym, W. P., Fabbiano, G., Elvis, M., et al. 2017, *ApJ*, **844**, 69
- Maksym, W. P., Fabbiano, G., Elvis, M., et al. 2019, *ApJ*, **872**, 94
- Malkan, M. A., Gorjian, V., & Tam, R. 1998, *ApJS*, **117**, 25
- Massaro, E., Giommi, P., Leto, C., et al. 2009, *A&A*, **495**, 691
- McMullin, J. P., Waters, B., Schiebel, D., Young, W., & Golap, K. 2007, in ASP Conf. Ser. 376, CASA Architecture and Applications, ed. R. A. Shaw, F. Hill, & D. J. Bell (San Francisco, CA: ASP), 127
- Medling, A. M., Privon, G. C., Barcos-Muñoz, L., et al. 2019, *ApJL*, **885**, L21
- Mezcua, M., Prieto, M. A., Fernández-Ontiveros, J. A., et al. 2015, *MNRAS*, **452**, A128
- Michiyama, T., Inoue, Y., & Doi, A. 2023, arXiv:2306.15950
- Morganti, R., Holt, J., Saripalli, L., Oosterloo, T. A., & Tadhunter, C. N. 2007, *A&A*, **476**, 735
- Morganti, R., Oosterloo, T., Oonk, J. B. R., Frieswijk, W., & Tadhunter, C. 2015, *A&A*, **580**, A1
- Morganti, R., Tsvetanov, Z. I., Gallimore, J., & Allen, M. G. 1999, *A&AS*, **137**, 457
- Mulchaey, J. S., Wilson, A. S., Bower, G. A., et al. 1994, *ApJ*, **433**, 625
- Mundell, C. G., Ferruit, P., Nagar, N., & Wilson, A. S. 2009, *ApJ*, **703**, 802
- Mundell, C. G., Holloway, A. J., Pedlar, A., et al. 1995, *MNRAS*, **275**, 67
- Muxlow, T. W. B., Pedlar, A., Holloway, A. J., Gallimore, J. F., & Antonucci, R. R. J. 1996, *MNRAS*, **278**, 854
- Nagar, N. M., Wilson, A. S., Mulchaey, J. S., & Gallimore, J. F. 1999, *ApJS*, **120**, 209
- Novak, M., Smolčić, V., Delhaize, J., et al. 2017, *A&A*, **602**, A5
- Orienti, M., & Prieto, M. A. 2010, *MNRAS*, **401**, 2599
- Paliya, V. S., Koss, M., Trakhtenbrot, B., et al. 2019, *ApJ*, **881**, 154
- Panessa, F., Baldi, R. D., Laor, A., et al. 2019, *NatAs*, **3**, 387
- Puccetti, S., Comastri, A., Bauer, F. E., et al. 2016, *A&A*, **585**, A157
- Ricci, C., Bauer, F. E., Treister, E., et al. 2017c, *MNRAS*, **468**, 1273
- Ricci, C., Chang, C.-S., Kawamuro, T., et al. 2023, *ApJL*, **952**, L28
- Ricci, C., Privon, G. C., Pfeifle, R. W., et al. 2021, *MNRAS*, **506**, 5935
- Ricci, C., Trakhtenbrot, B., Koss, M. J., et al. 2017a, *Natur*, **549**, 488
- Ricci, C., Trakhtenbrot, B., Koss, M. J., et al. 2017b, *ApJS*, **233**, 17
- Ricci, C., Ueda, Y., Koss, M. J., et al. 2015, *ApJL*, **815**, L13
- Ricci, T. V., Steiner, J. E., May, D., Garcia-Rissmann, A., & Menezes, R. B. 2018, *MNRAS*, **473**, 5334
- Sakamoto, K., Ho, P. T. P., Mao, R.-Q., Matsushita, S., & Peck, A. B. 2007, *ApJ*, **654**, 782
- Sandqvist, A., Jorsater, S., & Lindblad, P. O. 1982, *A&A*, **110**, 336
- Schmitt, H. R., Donley, J. L., Antonucci, R. R. J., Hutchings, J. B., & Kinney, A. L. 2003, *ApJS*, **148**, 327
- Schmitt, H. R., Ulvestad, J. S., Antonucci, R. R. J., & Kinney, A. L. 2001, *ApJS*, **132**, 199
- Scoville, N. Z., Evans, A. S., Thompson, R., et al. 2000, *AJ*, **119**, 991
- She, R., Ho, L. C., & Feng, H. 2017, *ApJ*, **835**, 223
- Shin, J., Woo, J.-H., Kim, M., & Wang, J. 2021, *ApJ*, **908**, 81
- Soifer, B. T., Bock, J. J., Marsh, K., et al. 2003, *AJ*, **126**, 143
- Stevens, I. R., Forbes, D. A., & Norris, R. P. 1999, *MNRAS*, **306**, 479
- Tanimoto, A., Ueda, Y., Kawamuro, T., et al. 2018, *ApJ*, **853**, 146
- Thean, A., Pedlar, A., Kukula, M. J., Baum, S. A., & O'Dea, C. P. 2000, *MNRAS*, **314**, 573
- Travascio, A., Fabbiano, G., Paggi, A., et al. 2021, *ApJ*, **921**, 129
- Treister, E., Messias, H., Privon, G. C., et al. 2020, *ApJ*, **890**, 149
- Tristram, K. R. W., Burtscher, L., Jaffe, W., et al. 2014, *A&A*, **563**, A82
- Tully, R. B., Rizzi, L., Shaya, E. J., et al. 2009, *AJ*, **138**, 323
- Ulvestad, J. S., & Wilson, A. S. 1983, *ApJL*, **264**, L7
- Wold, M., & Galliano, E. 2006, *MNRAS*, **369**, L47
- Wright, E. L., Eisenhardt, P. R. M., Mainzer, A. K., et al. 2010, *AJ*, **140**, 1868
- Zhao, Y., Lu, N., Xu, C. K., et al. 2016, *ApJ*, **820**, 118